Balance in Inequality: Testing the Physical Equilibrium, Precession, and Structural Stability of Magic Gems

Kyle Elliott Mathewson
Faculty of Science, University of Alberta
kyle.mathewson@ualberta.ca

Abstract

A magic square is a combinatorial paradigm of *balance in inequality*: its n^2 entries $\{1, \dots, n^2\}$ are strictly distinct, yet every row, column, and main diagonal sums to the same constant $\mu_n = n(n^2+1)/2$. Lifting the centred grid cells into $\mathbb{R}^3$ as radial vectors $\mathbf{p}_{ij}(\lambda) = (x_j, y_i, \lambda z_{ij})$ and taking their convex hull—the *Magic Gem* $\mathcal{G}_\lambda(S)$—raises a central mechanical question: when does combinatorial line-sum equality suffice for physical equilibrium in three dimensions, and when a nonlinear physical realization breaks that balance, how can an opposing inequality restore it? We test this principle across all 880 order-four magic squares by progressing from one-dimensional radial spokes to three-dimensional rotation, continuous solid and skeletal hulls, and freestanding stacked columns. For radial spokes from the origin O, natural vector lengths balance identically, whereas trimming the spokes to equal unit length breaks equilibrium on all 832 non-associative squares in 3D and on every square in 2D, where the irrational ring-radius ratio $r_2/r_1 = \sqrt{5}$ bounds the resultant below by the Pell convergent $9/4 \approx \sqrt{5}$ ($18\sqrt{10}/5 - 8\sqrt{2} \approx 0.0705$). By length–weight duality, radial equilibrium is restored either by assigning positive unequal tip weights $\mathbf{w}^* > \mathbf{0}$ on the unit sphere S^2 or by scaling spoke lengths as a power law (r^{α^*} in 2D and cubic vertical vanishing $(\mathbf{V}_3)_z = 0$ in 3D). In three-dimensional rotation, equal point masses at the unequal vertices $\mathbf{p}_{ij}(\lambda)$ make every semi-magic square an axisymmetric top with universal inertia ratio $I_\perp(\lambda)/I_{zz} = \frac{1}{2}(1 + \lambda^2(n^2+1))$ and spherical-top transition $\lambda_{\text{iso}} = (n^2+1)^{-1/2}$, whereas weighting the vertices by their unequal entries $m_{ij} = s_{ij}$ exposes the quadrant quadrupole $Q_{xy} = \sum z_{ij} x_j y_i$, splitting the horizontal principal moments by $2|Q_{xy}|$ and triggering 180° Dzhanibekov flips on 824 squares. Passing from discrete points to the uniform solid hull $\mathcal{G}_0(S)$ shifts the centre of mass off O on 829 squares because interior grid points $P_S^{(1)}$ are omitted and hull facets are weighted by unequal simplex volumes; because the outer hull vertices and inner core points pull in strictly opposite directions ($V_0 \overline{\mathbf{p}}_{\text{outer}} + V_1 \overline{\mathbf{p}}_{\text{inner}} = \mathbf{0}$), re-engaging the inner core $\mathcal{G}_1(S) = \operatorname{conv} P_S^{(1)}$ restores balance via two-density core inclusions, two-gauge nested wireframes, or the complete $\binom{n^2}{2}$-rod network K_{n^2} ($\Sigma_{\text{rods}} = \frac{2n^2-3}{3(n^2-1)}\Sigma(\lambda)$), while every boundary hull unfolds into a non-overlapping papercraft net with $f_0 - 1$ glue tabs. Finally, compressing the vertical aspect to the cubic print scale $\lambda = 1/5$ stabilizes 74.5% of all gem facets on a flat table, and alternating any gem $\mathcal{G}_\lambda(S)$ with its inverted mirror twin $\mathcal{G}_\lambda(r^2 S) = -\mathcal{G}_\lambda(S)$ cancels opposing facet tilts to lock chiral blocks into a straight vertical tower.

Keywords: magic squares; convex polyhedra; Albrecht Dürer; centre of mass; rigid-body precession; Dzhanibekov effect; polyhedral nets; mathematical sculpture.
MSC 2020: 52B10, 05B15, 70E15, 00A66.

1 Introduction: Balance in Inequality

Over five centuries ago, Albrecht Dürer contributed two enduring landmarks at the intersection of mathematics and the visual arts: the order-four magic square in his 1514 engraving *Melencolia I* (square #175 in Frénicle's 1693 census of the 880 order-four magic squares [8, 6, 1]) and the first printed polyhedral net unfoldings in his 1525 treatise *Underweysung der Messung* [7, 18, 5, 9]. A

magic square is a quintessential study in *balance in inequality*: an arrangement $S = (s_{ij})_{0\le i,j<n}$ of the first $N = n^2$ positive integers $\{1, \dots, N\}$ in which no two cells are equal, yet every row, column, and main diagonal sums to the exact same magic constant $\mu_n = n(N+1)/2$ (a *semi-magic square* if the row and column sums equal μ_n). Measuring coordinates from the board centre and the mean entry $\bar{s} = (N+1)/2$,

$$x_j = j - \frac{n-1}{2}, \qquad y_i = \frac{n-1}{2} - i, \qquad z_{ij} = s_{ij} - \frac{N+1}{2}, \tag{1}$$

lifts each cell (i, j) into a three-dimensional point and radial vector from the origin $O = (0, 0, 0)$:

$$\mathbf{p}_{ij}(\lambda) = (x_j,\, y_i,\, \lambda z_{ij}) \in \mathbb{R}^3, \qquad P_S(\lambda) = \big\{\mathbf{p}_{ij}(\lambda) : 0 \le i, j < n\big\},$$

where $\lambda > 0$ is the vertical lift scale (Figure 3(a)). The convex hull

$$\mathcal{G}_\lambda(S) := \operatorname{conv} P_S(\lambda) \subset \mathbb{R}^3 \qquad \big(\mathcal{G}(S) := \mathcal{G}_1(S)\big)$$

is a three-dimensional convex polyhedron that we call the *Magic Gem* of S, reuniting Dürer's magic squares with his polyhedral geometry.

In the flat grid plane, Loly [11] and Rogers and Loly [16, 17] showed that interpreting the unequal entries s_{ij} as point masses at $\mathbf{r}_{ij} = (x_j, y_i)$ places the planar centre of mass at the origin O ($\sum_{i,j} z_{ij}\mathbf{r}_{ij} = \mathbf{0}$) and makes the polar moment of inertia $\sum_{i,j} s_{ij}(x_j^2 + y_i^2) = n^2(n^4-1)/12$ invariant across all semi-magic squares of order n. When a lifted magic square is fabricated as a three-dimensional physical object—whether as a radial spoke star, a planar balance wheel, a spinning top on a pivot, a cast solid, a 3D-printed wireframe, a folded papercraft shell, or a freestanding tower of blocks [12]—its unequal entries are subjected to progressively nonlinear geometric transformations. This motivates our central hypothesis: *combinatorial line-sum equality guarantees physical equilibrium whenever a mechanical observable is linear or symmetric-quadratic in the grid coordinates, neutralizing entry inequality universally across all* 880 *order-four magic squares; when a nonlinear geometric constraint breaks that equilibrium, balance can be restored by pairing two opposing inequalities that cancel each other.*

We test this hypothesis across four progressive mechanical regimes, illustrated on six recurring flagship squares (Figure 1). In Section 2, we examine one-dimensional radial spoke sculptures radiating from the origin O. At natural spoke lengths, every magic square balances at O because unequal lengths compensate unequal directions. Trimming all sixteen spokes to equal unit length breaks equilibrium on all 832 non-associative squares in 3D and on *every* square in 2D, where the middle grid ring sits at an irrational radius ratio $r_2/r_1 = \sqrt{5}$ relative to the inner and outer rings ($r_3/r_1 = 3$) and prevents exact cancellation beyond the Pell convergent $9/4 \approx \sqrt{5}$ (square #70, Figure 1(b), Theorem 2.3). By length–weight duality (Proposition 2.2), equilibrium is restored either by playing aligned inner and outer ring dipoles against the middle ring via a power-law length profile r^{α^*} (such as $\alpha^* = -1$ on #45, Figure 1(c), Corollary 2.4), or by assigning positive unequal tip weights $\mathbf{w}^* > \mathbf{0}$ on the unit sphere S^2 and cubic spoke lengths ($\beta = 3$, where the vertical resultant vanishes universally, Theorem 2.5).

In Section 3, we set balanced sculptures into three-dimensional rotation on a central pivot under gravity. When the sixteen unequal vertices $\mathbf{p}_{ij}(\lambda)$ carry equal masses, line-sum equality eliminates all off-diagonal products of inertia, turning every semi-magic square into a smooth axisymmetric top that passes through an exact spherical-top transition at $\lambda_{\text{iso}} = (n^2+1)^{-1/2}$ ($1/\sqrt{17}$ at $n = 4$, Theorem 3.1). Replacing equal masses with the unequal magic entries $m_{ij} = s_{ij}$ (Theorem 3.2) breaks this rotational symmetry by exposing the planar quadrupole moment $Q_{xy} = \sum z_{ij}x_jy_i$ and the cubic vector resultant from Section 2, splitting the horizontal principal axes by $2|Q_{xy}|$ and triggering 180° Dzhanibekov flips on 824 of the 880 squares (led by #46 at $|Q_{xy}| = 60$, Figure 1(d)).

In Section 4, we pass from discrete point clouds to continuous polyhedral hulls $\mathcal{G}_0(S) = \operatorname{conv} P_S$. Casting $\mathcal{G}_0(S)$ as a uniform solid preserves near-axisymmetric inertia about its own centroid $\mathbf{c}_0(S)$, but shifts $\mathbf{c}_0(S)$ off the pivot O on 829 of the 880 squares (51 balance naturally, Proposition 4.1)

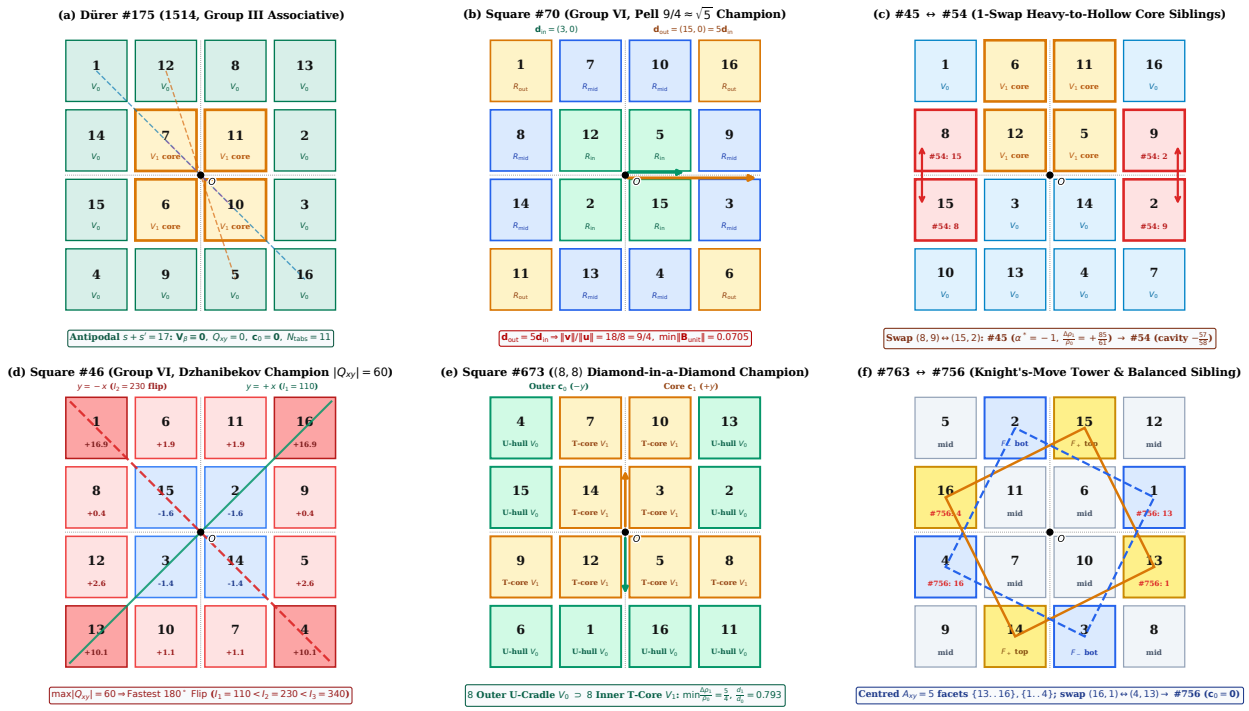


Figure 1: Visual anatomy of the six flagship order-four magic squares examined across Sections 2–5. (a) Dürer's associative square #175 (1514, Group III), whose antipodal pairs sum to 17 across O, partitioning into 12 outer hull vertices V_0 and 4 inner core vertices V_1. (b) Square #70 (Group VI), coloured by concentric rings $R_{\text{in}}, R_{\text{mid}}, R_{\text{out}}$, where parallel ring dipoles $\mathbf{d}_{\text{out}} = 5\mathbf{d}_{\text{in}}$ achieve the Pell ratio $9/4 \approx \sqrt{5}$, and (c) square #45 ($\kappa = +9$, $\alpha^* = -1$), whose single border swap $(8, 9) \leftrightarrow (15, 2)$ flips a heavy-core gem into hollow-cavity sibling #54. (d) Square #46 (Group VI), shaded by quadrant quadrupole $z_i x_j y_i$, attaining the maximum $|Q_{xy}| = 60$ and fastest 180° Dzhanibekov flip about $y = -x$. (e) Square #673 (Group VI), whose 8-vertex U-cradle V_0 encloses an 8-vertex inverted-T core V_1 ($\Delta\rho_1/\rho_0 = 5/4$), and (f) square #763 (Group VI), whose centred knight's-move facets $\{13, 14, 15, 16\}$ and $\{1, 2, 3, 4\}$ lock into an area-5 mirror-twin tower.

because interior grid points $P_S^{(1)}$ are omitted and boundary facets are weighted by unequal simplex volumes. Because $\sum \mathbf{p}_{ij} = \mathbf{0}$, the outer hull vertices and the inner core points pull in strictly opposite directions across the origin ($V_0\overline{\mathbf{p}}_{\text{outer}} = -V_1\overline{\mathbf{p}}_{\text{inner}}$, Proposition 4.2). Physically re-engaging the inner core $\mathcal{G}_1(S) = \text{conv}\, P_S^{(1)}$ restores $\mathbf{c} = \mathbf{0}$ across composite solids (such as denser-core gem #673 and hollow-cavity gem #54, Figure 1(c,e), Theorem 4.3), single-material two-gauge wireframes and complete K_{16} strut networks (Theorem 4.4), and unfolded papercraft shells with $f_0 - 1$ glue tabs (Proposition 4.5).

Finally, in Section 5, we remove the central pivot and place Magic Gems onto a flat horizontal table under gravity. While tall $\lambda = 1$ gems topple on more than half of their facets, compressing the vertical lift to the cubic print scale $\lambda_{\text{cube}} = 1/5$ stabilizes 74.5% of all 14,824 facets (Proposition 5.2). When stacking multiple blocks vertically, identical copies of a single gem wedge apart whenever the top and bottom facet normals fail to oppose ($\mathbf{n}_- \neq -\mathbf{n}_+$ on 756 gems); alternating $\mathcal{G}_\lambda(S)$ with its inverted mirror twin $\mathcal{G}_\lambda(r^2\overline{S}) = -\mathcal{G}_\lambda(S)$ (Theorem 5.3) pairs every slanted facet with an equal and opposite partner, locking chiral knight's-move blocks (#763, Figure 1(f)) into a straight vertical column (Proposition 5.4).

Across all four regimes, the order-four censuses stratify into three symmetry tiers (Section 6): universal properties governed by linear line sums hold across all 880 squares; unweighted nonlinear cancellations hold on the 48 associative squares of Dudeney's Group III ($r^2 S = \overline{S}$, led by Dürer's #175), where central inversion $\mathbf{p}_{-c} = -\mathbf{p}_c$ cancels opposite cells pairwise; and one-parameter counterbalancing between opposing rings or hull layers occurs in the 304 self-complementary squares of Dudeney's Group VI ($\overline{S} = hS$ or vS), where a 180° half-turn symmetry ($C_2 \subset SO(3)$) confines

residual imbalance vectors to a single coordinate axis. Every theorem and census table is certified in exact rational arithmetic by `anc/verify_paper_c.py` (Section A) and accompanied by real-time 3D simulations in `web/index.html`.

Throughout the paper, $A_n = \{(x_j, y_i) : 0 \le i, j < n\}$ denotes the centred grid (1), $a_n = (n^2-1)/12$ and $b_n = (n^4-1)/12 = (n^2+1)a_n$ denote the marginal variances of x_j and z_{ij}, and the dihedral group $D_4 = \langle r, h\rangle$ (with 90° rotation r and reflections h, v) acts on arrangements together with the complement involution $\tau(S) = \overline{S} = (N+1)\mathbf{1} - S$. Companion preprints [14, 13] treat the static polyhedral combinatorics and bivariate Prouhet–Tarry–Escott moment hierarchy of semi-magic squares; the present paper is self-contained. Order-four magic squares are numbered #1, ..., #880 by their 1-based position in Frénicle's standard list (`anc/squares880.txt`).

2 Radial Spokes from the Origin and Length–Weight Duality

In the fabrication suite `magicGemWeb` [12], the sixteen cells of an order-four magic square are built as two radial sculptures pivoted at the origin O: a three-dimensional sixteen-spoke hub-and-strut star (`magicGem.scad`, Figure 3(a)) with spokes $\mathbf{p}_{ij}(\lambda) = (x_j, y_i, \lambda z_{ij})$ of length $R_{ij}(\lambda) = \|\mathbf{p}_{ij}(\lambda)\|_2$ along unit directions $\hat{\mathbf{p}}_{ij}(\lambda) = \mathbf{p}_{ij}(\lambda)/R_{ij}(\lambda) \in S^2$, and a planar sixteen-spoke balance wheel on a conical fulcrum (`weighted_ring.stl`, Figure 2(a)) with spokes along $\mathbf{r}_{ij} = (x_j, y_i)$ of radius $r_{ij} = \|\mathbf{r}_{ij}\|_2$ and unit direction $\mathbf{u}_{ij} = \mathbf{r}_{ij}/r_{ij} \in S^1$. At natural linear lengths ($L_{ij} = R_{ij}(\lambda)$ or $\ell(r_{ij}) = r_{ij}$), both sculptures balance identically at O because $\sum_{i,j} \mathbf{p}_{ij}(\lambda) = \mathbf{0}$ and $\sum_{i,j} z_{ij}\mathbf{r}_{ij} = \mathbf{0}$ [11, 17], closing the sixteen planar vectors into a head-to-tail polygon (Figure 2(b)).

Our first test probes the mechanism of this equilibrium: does radial balance reside in the directions of the spokes alone, or does it rely on the unequal spoke lengths compensating the unequal directions? And when equalizing spoke lengths breaks balance, how can an opposing inequality in tip weights or power-law lengths restore it?

2.1 Length–Weight Duality: Why Equalizing Spoke Lengths Breaks Balance

Definition 2.1 (Generalized 3D and planar origin-vector resultants)**.** For an arrangement S of order n and vertical lift scale $\lambda > 0$, let $R_{ij}(\lambda) = \sqrt{x_j^2 + y_i^2 + \lambda^2 z_{ij}^2}$ and $\hat{\mathbf{p}}_{ij}(\lambda) = \mathbf{p}_{ij}(\lambda)/R_{ij}(\lambda)$ ($\mathbf{0}$ if $R_{ij}(\lambda) = 0$). Given cell weights $w = (w_{ij})$ and prescribed 3D spoke lengths $L = (L_{ij})$, the *3D origin-vector resultant* is

$$\mathbf{V}_{w,L}(S;\lambda) = \sum_{i,j} w_{ij}\, L_{ij}\, \hat{\mathbf{p}}_{ij}(\lambda) = \sum_{R_{ij}(\lambda)>0} \left(\frac{w_{ij} L_{ij}}{R_{ij}(\lambda)}\right) \mathbf{p}_{ij}(\lambda) \in \mathbb{R}^3. \tag{2}$$

For equal weights $w_{ij} = 1$ and power-law 3D lengths $L_{ij} = R_{ij}(\lambda)^\beta$ ($\beta \in \mathbb{R}$), we write

$$\mathbf{V}_\beta(S;\lambda) := \sum_{i,j} R_{ij}(\lambda)^\beta\, \hat{\mathbf{p}}_{ij}(\lambda) = \sum_{i,j} R_{ij}(\lambda)^{\beta-1}\, \mathbf{p}_{ij}(\lambda) \in \mathbb{R}^3, \tag{3}$$

and for weighted unit vectors ($L_{ij} = 1$) on S^2, we write $\mathbf{B}^{(3)}_{w,\lambda}(S) := \mathbf{V}_{w,1}(S;\lambda) = \sum_{i,j} w_{ij}\hat{\mathbf{p}}_{ij}(\lambda)$. Similarly, in the grid plane, given cell masses $m = (m_{ij})$ and a radial length profile $\ell\colon [0,\infty) \to [0,\infty)$ along unit rays $\mathbf{u}_{ij} = \mathbf{r}_{ij}/r_{ij}$, the *planar radial resultant* is

$$\mathbf{B}_{m,\ell}(S) = \sum_{i,j} m_{ij}\, \ell(r_{ij})\, \mathbf{u}_{ij} = \sum_{r_{ij}>0} \left(\frac{m_{ij}\ell(r_{ij})}{r_{ij}}\right) (x_j, y_i) \in \mathbb{R}^2. \tag{4}$$

Because $\ell(r_{ij})$ depends only on the radius r_{ij}, grid symmetry gives $\sum_{i,j} \ell(r_{ij})\mathbf{u}_{ij} = \mathbf{0}$, so replacing the positive entry masses $m_{ij} = s_{ij} = \bar{s} + z_{ij}$ by the signed heights $m_{ij} = z_{ij}$ leaves the planar resultant unchanged: $\mathbf{B}_{s,\ell}(S) = \mathbf{B}_{z,\ell}(S)$.

Proposition 2.2 (Length–weight duality and the order-three two-ring law)**.** *Let $n \geq 3$ and $\lambda > 0$. Scaling 3D vector lengths from the origin to L_{ij} with weights w_{ij} produces the same resultant (2) as keeping the natural 3D vectors $\mathbf{p}_{ij}(\lambda)$ ($L'_{ij} = R_{ij}(\lambda)$) and assigning effective weights $w'_{ij} = w_{ij}L_{ij}/R_{ij}(\lambda)$. In particular, power-law 3D spoke lengths $L_{ij} = R_{ij}(\lambda)^{\beta}$ with unit weights ($w_{ij} = 1$) are mechanically dual to natural 3D vectors $\mathbf{p}_{ij}(\lambda)$ with weights $w'_{ij} = R_{ij}(\lambda)^{\beta-1}$, and unit-length 3D vectors on S^2 ($L_{ij} = 1$) balance identically ($\sum_{i,j} w_{ij}\hat{\mathbf{p}}_{ij}(\lambda) = \mathbf{0}$) for every arrangement S when weighted by their unequal 3D lengths $w_{ij} = c\,R_{ij}(\lambda)$ ($c \in \mathbb{R}$). In the grid plane, unit vectors $\mathbf{u}_{ij}$ balance for every semi-magic square ($\sum_{i,j} m_{ij}\mathbf{u}_{ij} = \mathbf{0}$) whenever $m_{ij} = c\,z_{ij}r_{ij}$, and a radial profile ℓ_{ij} with $m_{ij} = z_{ij}$ balances every semi-magic square if and only if $(\ell_{ij}/r_{ij})\mathbf{r}_{ij}$ has components in the row–column subspace $W_{\mathrm{rc}} = \{a(x_j) + b(y_i)\}$.*

At order $n = 3$, where the eight non-central cells of A_3 lie on two concentric rings—four edge midpoints $R_1 = \{(\pm1, 0), (0, \pm1)\}$ ($r_1 = 1$) and four corners $R_{\sqrt{2}} = \{(\pm1, \pm1)\}$ ($r_2 = \sqrt{2}$)—every semi-magic square S satisfies $\mathbf{d}_1(S) + \mathbf{d}_2(S) = \mathbf{0}$ for $\mathbf{d}_k(S) = \sum_{(i,j)\in R_k} z_{ij}\mathbf{r}_{ij}$, and hence

$$\mathbf{B}_{z,\ell}(S) = \left(\ell(1) - \frac{\ell(\sqrt{2})}{\sqrt{2}}\right)\mathbf{d}_1(S). \tag{5}$$

For all eight magic squares of order 3 (the D_4-orbit of the Lo Shu square), $\|\mathbf{d}_1(S)\|_2 = \sqrt{80} = 4\sqrt{5}$, giving

$$\|\mathbf{B}_{z,\ell}(S)\|_2 = 4\sqrt{5}\left|\ell(1) - \frac{\ell(\sqrt{2})}{\sqrt{2}}\right|, \qquad \|\mathbf{B}_{\mathrm{unit}}(S)\|_2 = 4\sqrt{5} - 2\sqrt{10} \approx 2.619717, \tag{6}$$

so $\mathbf{B}_{z,\ell}(S) = \mathbf{0}$ at $n = 3$ if and only if $\ell(\sqrt{2}) = \sqrt{2}\,\ell(1)$.

Proof. The duality relations follow directly from (2)–(4), the identity $\sum_{i,j} \mathbf{p}_{ij}(\lambda) = \mathbf{0}$, and the characterization of W_{rc} as the orthogonal complement of the zero-line-sum space [13, Sect. 2]. At order $n = 3$, $\mathbf{r}_{11} = (0, 0)$ implies $\mathbf{d}_1(S) + \mathbf{d}_2(S) = \sum_{i,j} z_{ij}\mathbf{r}_{ij} = \mathbf{0}$ for every semi-magic square, which yields (5) upon grouping (4) over R_1 and $R_{\sqrt{2}}$. Evaluating $\mathbf{d}_1 = (-8, 4)$ on the Lo Shu square gives $\|\mathbf{d}_1\|_2 = \sqrt{80} = 4\sqrt{5}$, and D_4-invariance of the Euclidean norm yields (6). □

Proposition 2.2 makes the mechanics of spoke normalization transparent: forcing unequal spokes to equal unit length ($L_{ij} = 1$ or $\ell = 1$) divides each coordinate vector by its irrational radius $R_{ij}(\lambda)$ or r_{ij}. At order $n = 3$, the corner ring sits at an irrational ratio $r_2/r_1 = \sqrt{2}$, so equalizing the spoke lengths breaks the cancellation between $\mathbf{d}_1$ and $\mathbf{d}_2 = -\mathbf{d}_1$. We now examine how this irrationality mechanism operates across the three concentric rings of order $n = 4$.

2.2 Planar Balance Wheels: The $\sqrt{5}$ Irrationality Barrier and Power-Law Restoration

At order $n = 4$, the sixteen cells of $A_4 = \{-\frac{3}{2}, -\frac{1}{2}, \frac{1}{2}, \frac{3}{2}\}^2$ partition into three concentric rings around the origin O (Figure 1(b), Figure 2(a)): four inner cells $R_{\mathrm{in}} = \{(\pm\frac{1}{2}, \pm\frac{1}{2})\}$ of radius $r_1 = \sqrt{2}/2$, eight middle edge-interior cells $R_{\mathrm{mid}} = \{(\pm\frac{3}{2}, \pm\frac{1}{2}), (\pm\frac{1}{2}, \pm\frac{3}{2})\}$ of radius $r_2 = \sqrt{10}/2$, and four outer corner cells $R_{\mathrm{out}} = \{(\pm\frac{3}{2}, \pm\frac{3}{2})\}$ of radius $r_3 = 3\sqrt{2}/2$. Whereas the outer and inner radii have a rational ratio $r_3/r_1 = 3$, the middle and inner radii have the irrational ratio $r_2/r_1 = \sqrt{5} \notin \mathbb{Q}$. Consequently, when spokes are trimmed to unit length ($\alpha = 0$), the inner and outer rings combine into an integer lattice vector $\mathbf{u}(S)$ that attempts to cancel an irrational multiple $\mathbf{v}(S)/\sqrt{5}$ from the middle ring.

Theorem 2.3 (Three-Ring Decomposition, Irrationality No-Go, and Pell Minimum)**.** *For any arrangement S of order 4, define the three ring dipole vectors radiating from O by $\mathbf{d}_{\mathrm{in}}(S) = \sum_{c\in R_{\mathrm{in}}} z_c\mathbf{r}_c$, $\mathbf{d}_{\mathrm{mid}}(S) = \sum_{c\in R_{\mathrm{mid}}} z_c\mathbf{r}_c$, and $\mathbf{d}_{\mathrm{out}}(S) = \sum_{c\in R_{\mathrm{out}}} z_c\mathbf{r}_c$. For every 4×4 arrangement S*

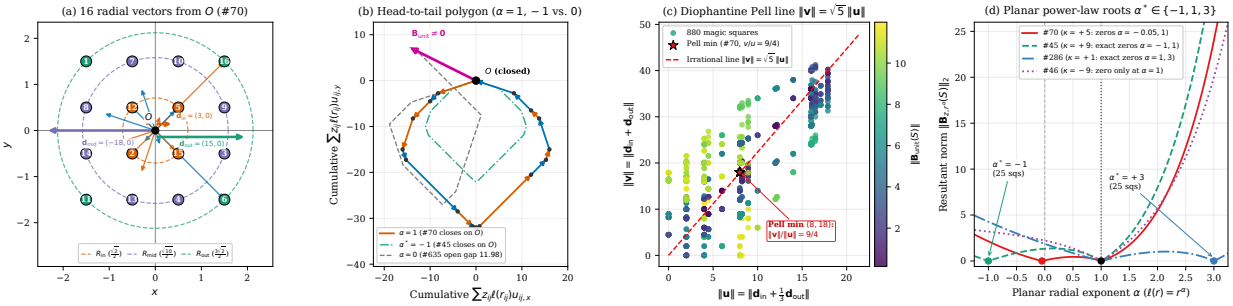


Figure 2: Planar radial vectors from the origin $O = (0, 0)$, head-to-tail polygon closure, and the Diophantine Pell minimum at order four. (a) Radial vectors $z_{ij}\mathbf{r}_{ij}$ on square #70 across the three concentric rings $R_{\text{in}}, R_{\text{mid}}, R_{\text{out}}$, with ring dipoles $\mathbf{d}_{\text{in}} = (3, 0)$, $\mathbf{d}_{\text{out}} = (15, 0)$, and $\mathbf{d}_{\text{mid}} = (-18, 0)$. (b) Ordered head-to-tail placement closes the 16-gon at linear lengths $\alpha = 1$ (#70) and inverse lengths $\alpha^* = -1$ (#45), whereas unit lengths $\alpha = 0$ (#635) leave a nonzero gap $\mathbf{B}_{\text{unit}}(S)$ (magenta). (c) Census of $\|\mathbf{v}(S)\|_2$ versus $\|\mathbf{u}(S)\|_2$ across all 880 squares against the irrational balance line $\|\mathbf{v}\| = \sqrt{5}\,\|\mathbf{u}\|$, with the eight Pell-minimum squares ($v/u = 9/4$) marked by red stars. (d) Resultant norm $\|\mathbf{B}_{z,r^\alpha}(S)\|_2$ versus exponent α, showing the universal zero at $\alpha = 1$ and second roots at $\alpha^* = -1$ (#45), -0.050 (#70), and $+3$ (#286).

of distinct integers, $\mathbf{d}_{\text{in}}(S) \neq \mathbf{0}$ *and* $\mathbf{d}_{\text{out}}(S) \neq \mathbf{0}$*; for every order-four magic square* $S \in \mathcal{M}_4$*, both* R_{in} *and* R_{out} *sum to* $\mu_4 = 34$*, so* $\mathbf{d}_{\text{in}}(S) \in \mathbb{Z}^2 \setminus \{\mathbf{0}\}$ *and* $\mathbf{d}_{\text{out}}(S) \in (3\mathbb{Z})^2 \setminus \{\mathbf{0}\}$ *satisfy*

$$\|\mathbf{d}_{\text{in}}(S)\|_2 \geq 1, \qquad \|\mathbf{d}_{\text{out}}(S)\|_2 \geq 3. \tag{7}$$

Whenever $\sum_{c \in A_4} z_c \mathbf{r}_c = \mathbf{0}$ *(in particular, for every semi-magic square),* $\mathbf{d}_{\text{mid}}(S) = -\big(\mathbf{d}_{\text{in}}(S) + \mathbf{d}_{\text{out}}(S)\big)$*, and for every radial length profile* $\ell = (\ell_1, \ell_2, \ell_3)$ *on* (r_1, r_2, r_3)*,*

$$\mathbf{B}_{z,\ell}(S) = \left(\frac{\ell_1}{r_1} - \frac{\ell_2}{r_2}\right)\mathbf{d}_{\text{in}}(S) + \left(\frac{\ell_3}{r_3} - \frac{\ell_2}{r_2}\right)\mathbf{d}_{\text{out}}(S). \tag{8}$$

In particular, for planar unit vectors ($\ell_1 = \ell_2 = \ell_3 = 1$*, i.e.* $\alpha = 0$)*,*

$$\mathbf{B}_{\text{unit}}(S) = \sqrt{2}\left(\mathbf{u}(S) - \frac{1}{\sqrt{5}}\,\mathbf{v}(S)\right), \tag{9}$$

where $\mathbf{u}(S) = \mathbf{d}_{\text{in}}(S) + \frac{1}{3}\mathbf{d}_{\text{out}}(S) \in \mathbb{Z}^2$ *and* $\mathbf{v}(S) = \mathbf{d}_{\text{in}}(S) + \mathbf{d}_{\text{out}}(S) = -\mathbf{d}_{\text{mid}}(S) \in \mathbb{Z}^2$*. Because* $\sqrt{5} \notin \mathbb{Q}$ *and* $\mathbf{d}_{\text{in}}(S), \mathbf{d}_{\text{out}}(S) \neq \mathbf{0}$*, no* 4×4 *arrangement of distinct integers with vanishing first moments (and hence no* 4×4 *semi-magic or magic square) ever satisfies* $\mathbf{B}_{\text{unit}}(S) = \mathbf{0}$*, nor can* $\mathbf{B}_{z,r^\alpha}(S) = \mathbf{0}$ *hold for any even integer* $\alpha \in 2\mathbb{Z}$*. Across all* 880 *magic squares of order* 4*, the global minimum of* $\|\mathbf{B}_{\text{unit}}(S)\|_2$ *is*

$$\min_{S \in \mathcal{M}_4} \|\mathbf{B}_{\text{unit}}(S)\|_2 = \frac{18\sqrt{10}}{5} - 8\sqrt{2} = \frac{2\sqrt{10}}{5(9 + 4\sqrt{5})} = \frac{2\sqrt{10}}{5\varphi^6} \approx 0.07049108, \tag{10}$$

where $\varphi = (1 + \sqrt{5})/2$*. This minimum is attained when* $\mathbf{d}_{\text{out}}(S) = 5\mathbf{d}_{\text{in}}(S)$ *with* $\|\mathbf{d}_{\text{in}}(S)\|_2 = 3$*, where* $\mathbf{u}(S)$ *and* $\mathbf{v}(S)$ *are parallel in the ratio* $\|\mathbf{v}\|/\|\mathbf{u}\| = 18/8 = 9/4$*, the fundamental Pell convergent to* $\sqrt{5}$ *(*$9^2 - 5 \cdot 4^2 = 1$*). Up to* D_4*-symmetry, exactly eight magic squares achieve* (10)*: squares #70, #76, #121, #188, #452, #459, #490, and #574, all in Dudeney's Group VI.*

Proof. Labelling the four entries of R_{in} at $(-\frac{1}{2}, \frac{1}{2})$, $(\frac{1}{2}, \frac{1}{2})$, $(-\frac{1}{2}, -\frac{1}{2})$, $(\frac{1}{2}, -\frac{1}{2})$ by $a, b, c, d \in \mathbb{Z}$ gives $\mathbf{d}_{\text{in}}(S) = \frac{1}{2}\big((b + d) - (a + c), (a + b) - (c + d)\big)$. If $\mathbf{d}_{\text{in}}(S) = \mathbf{0}$, then $b + d = a + c$ and $a + b = c + d$; adding and subtracting these equations forces $b = c$ and $a = d$, contradicting that S has distinct entries. For $S \in \mathcal{M}_4$, subtracting the sum of all sixteen cells ($4\mu_4$) from the sum of the two outer rows and two outer columns ($R_0 + R_3 + C_0 + C_3 = 4\mu_4$) gives $\sum_{c \in R_{\text{out}}} s_c - \sum_{c \in R_{\text{in}}} s_c = 0$, while the two main diagonals sum to $D_1 + D_2 = \sum_{c \in R_{\text{out}}} s_c + \sum_{c \in R_{\text{in}}} s_c = 2\mu_4$; hence $\sum_{c \in R_{\text{in}}} s_c =$

$\sum_{c\in R_{\text{out}}} s_c = \mu_4 = 34$ (an even integer), which implies $\mathbf{d}_{\text{in}}(S) \in \mathbb{Z}^2 \setminus \{\mathbf{0}\}$. Since the corner coordinates are $(\pm\frac{3}{2},\pm\frac{3}{2}) = 3(\pm\frac{1}{2},\pm\frac{1}{2})$, identical algebra gives $\mathbf{d}_{\text{out}}(S) \in (3\mathbb{Z})^2 \setminus \{\mathbf{0}\}$ and (7). Partitioning $A_4 = R_{\text{in}} \sqcup R_{\text{mid}} \sqcup R_{\text{out}}$ gives $\mathbf{d}_{\text{mid}} = -(\mathbf{d}_{\text{in}} + \mathbf{d}_{\text{out}})$, and substituting this relation into (4) yields (8).

Setting $\ell_1 = \ell_2 = \ell_3 = 1$ with $1/r_1 = \sqrt{2}$, $1/r_2 = \sqrt{2}/\sqrt{5}$, and $1/r_3 = \sqrt{2}/3$ in (8) gives $\mathbf{B}_{\text{unit}}(S) = (\sqrt{2} - \sqrt{2}/\sqrt{5})\mathbf{d}_{\text{in}} + (\sqrt{2}/3 - \sqrt{2}/\sqrt{5})\mathbf{d}_{\text{out}} = \sqrt{2}\big((\mathbf{d}_{\text{in}} + \frac{1}{3}\mathbf{d}_{\text{out}}) - \frac{1}{\sqrt{5}}(\mathbf{d}_{\text{in}} + \mathbf{d}_{\text{out}})\big)$, which is (9). Because $\mathbf{u}(S), \mathbf{v}(S) \in \mathbb{Z}^2$ and $\sqrt{5} \notin \mathbb{Q}$, $\mathbf{B}_{\text{unit}}(S) = \mathbf{0}$ requires $\mathbf{u}(S) = \mathbf{v}(S) = \mathbf{0}$, which forces $\mathbf{d}_{\text{in}}(S) = \mathbf{d}_{\text{out}}(S) = \mathbf{0}$, a contradiction. The same irrationality holds for any even exponent $\alpha = 2m$, where $r_2^{\alpha-1}/r_1^{\alpha-1} = 5^{m-1}\sqrt{5} \notin \mathbb{Q}$.

To establish the Pell minimum (10), subtracting $C_1 + C_2 = 2\mu_4$ and $C_0 + C_3 = 2\mu_4$ from $D_1 + D_2 = 2\mu_4$ gives $s_{00} + s_{03} = s_{31} + s_{32}$ and $s_{11} + s_{12} = s_{20} + s_{23}$; across all 24 modulo-2 parity patterns of $\mathcal{M}_4$, the four top diagonal cells $T_{\text{diag}} = \{(0,0),(0,3),(1,1),(1,2)\}$ (and likewise $R_{\text{diag}} = \{(0,3),(3,3),(1,2),(2,2)\}$) always have an even sum $\sum_{c\in T_{\text{diag}}} s_c \in \{18, 20, \ldots, 42\}$. Since $u_y(S) = \sum_{c\in T_{\text{diag}}} s_c - 34$, $u_x(S) = \sum_{c\in R_{\text{diag}}} s_c - 34$, and $\mathbf{v}(S) - \mathbf{u}(S) = \frac{2}{3}\mathbf{d}_{\text{out}}(S) \in (2\mathbb{Z})^2$, every magic square $S \in \mathcal{M}_4$ satisfies $\mathbf{u}(S) = 2\tilde{\mathbf{u}}(S) \in (2\mathbb{Z})^2$ and $\mathbf{v}(S) = 2\tilde{\mathbf{v}}(S) \in (2\mathbb{Z})^2$ with $\tilde{\mathbf{u}}(S), \tilde{\mathbf{v}}(S) \in \mathbb{Z}^2 \setminus \{\mathbf{0}\}$, $\|\tilde{\mathbf{u}}(S)\|_\infty \le 8$, and $\|\tilde{\mathbf{u}}(S)\|_2 \le 4\sqrt{5} < 9$. Consequently, (9) becomes $\|\mathbf{B}_{\text{unit}}(S)\|_2 = 2\sqrt{2}\,\|\tilde{\mathbf{u}}(S) - \tilde{\mathbf{v}}(S)/\sqrt{5}\|_2$. Decomposing $\tilde{\mathbf{v}}$ parallel and orthogonal to $\tilde{\mathbf{u}}$ shows that this norm is minimized when $\tilde{\mathbf{u}} = \tilde{u}\mathbf{e}$ and $\tilde{\mathbf{v}} = \tilde{v}\mathbf{e}$ lie along a coordinate axis $\mathbf{e} \in \{\pm\hat{\mathbf{e}}_x, \pm\hat{\mathbf{e}}_y\}$ ($\|\mathbf{e}\|_2 = 1$) with $1 \le \tilde{u} \le 8$. By Lagrange's theorem on continued fractions for $\sqrt{5} = [2;\overline{4}]$ (whose principal convergents are $2/1, 9/4, 38/17, \ldots$), across all integer denominators $1 \le \tilde{u} \le 8 < 17$ the unique best rational approximation to $\sqrt{5}$ is the fundamental Pell convergent $\tilde{v}/\tilde{u} = 9/4$ ($9^2 - 5\cdot 4^2 = 1$), corresponding to $(u,v) = (8,18)$ ($\mathbf{d}_{\text{out}} = 5\mathbf{d}_{\text{in}}$ with $\|\mathbf{d}_{\text{in}}\|_2 = 3$) and giving $2\sqrt{2}(9/\sqrt{5} - 4) = 18\sqrt{10}/5 - 8\sqrt{2} = 2\sqrt{10}/(5\varphi^6) \approx 0.07049108$. On square #70 (Figure 1(b)), the inner ring $\{5, 12, 2, 15\}$ gives $\mathbf{d}_{\text{in}} = (3,0)$ and the outer corners $\{1, 16, 11, 6\}$ give $\mathbf{d}_{\text{out}} = (15,0) = 5\mathbf{d}_{\text{in}}$, realizing $\mathbf{u} = (8,0)$, $\mathbf{v} = (18,0)$, and (10). □

How, then, can a planar balance wheel achieve exact equilibrium at a non-linear length profile $\ell(r) = r^\alpha$ ($\alpha \ne 1$)? Equation (8) shows that balance is restored whenever the inner and outer ring dipoles align in the same direction ($\mathbf{d}_{\text{out}} = \kappa\mathbf{d}_{\text{in}}$ with $\kappa > 0$), so that both rings jointly oppose the middle ring $\mathbf{d}_{\text{mid}} = -(1+\kappa)\mathbf{d}_{\text{in}}$ (Figure 2(d)).

Corollary 2.4 (Restoring planar balance via power-law exponents $\alpha^* \ne 1$)**.** *For power-law radial lengths $\ell(r) = r^\alpha$ ($\alpha \in \mathbb{R}$), equation (8) takes the form*

$$\mathbf{B}_{z,r^\alpha}(S) = r_1^{\alpha-1}\Big[\big(1 - 5^{(\alpha-1)/2}\big)\mathbf{d}_{\text{in}}(S) + \big(3^{\alpha-1} - 5^{(\alpha-1)/2}\big)\mathbf{d}_{\text{out}}(S)\Big]. \tag{11}$$

Because $1 < \sqrt{5} < 3$, the ratio $h(\alpha) = \frac{5^{(\alpha-1)/2}-1}{3^{\alpha-1}-5^{(\alpha-1)/2}}$ (extended by $h(1) = \frac{\ln 5}{\ln(9/5)} \approx 2.7381$) is a strictly decreasing bijection from $\mathbb{R}$ onto $(0,\infty)$. Consequently, an order-four magic square S possesses a second power-law balance exponent $\alpha^*(S) \ne 1$ satisfying $\mathbf{B}_{z,r^{\alpha^*}}(S) = \mathbf{0}$ if and only if $\mathbf{d}_{\text{in}}(S)$ and $\mathbf{d}_{\text{out}}(S)$ are strictly parallel ($\mathbf{d}_{\text{out}}(S) = \kappa\mathbf{d}_{\text{in}}(S)$ with $\kappa > 0$), which holds for 204 of the 880 magic squares (while 204 squares have anti-parallel dipoles $\kappa < 0$). Across all 880 magic squares, the second root $\alpha^*(\kappa)$ is an integer in only two cases: inverse radial lengths $\alpha^* = -1$ ($\ell(r) = 1/r$, corresponding to $\kappa = h(-1) = +9$), achieved by 25 squares including #45 (Figure 1(c)), and cubic radial lengths $\alpha^* = +3$ ($\ell(r) = r^3$, corresponding to $\kappa = h(3) = +1$), achieved by 25 squares including #286. For the 17 squares with $\kappa = +5$ (including the eight Pell-minimum squares of Theorem 2.3), the exact zero occurs at $\alpha^*(5) \approx -0.0496$, explaining why $\|\mathbf{B}_{z,r^\alpha}(S)\|_2$ pinches nearly to zero at $\alpha = 0$ (Figure 2(d)).

Proof. Setting (11) to $\mathbf{0}$ for $\alpha \ne 1$ requires $\mathbf{d}_{\text{out}}(S) = h(\alpha)\mathbf{d}_{\text{in}}(S)$. Since $1 < 5^{t/2} < 3^t$ for $t = \alpha - 1 > 0$ and $3^t < 5^{t/2} < 1$ for $t < 0$, both numerator and denominator of $h(\alpha)$ have the sign of $\alpha - 1$, so $h(\alpha) > 0$ with $\lim_{\alpha\to-\infty} h(\alpha) = +\infty$ and $\lim_{\alpha\to+\infty} h(\alpha) = 0$. Since $\kappa \in \mathbb{Q}_{>0}$ cannot equal the transcendental number $\frac{\ln 5}{\ln(9/5)}$, every square with $\kappa > 0$ has a unique root $\alpha^*(\kappa) = h^{-1}(\kappa) \ne 1$. By Theorem 2.3, an integer root $\alpha^* \ne 1$ must be odd, $\alpha^* = 2m + 1$ ($m \in \mathbb{Z} \setminus \{0\}$), where

$h(2m+1) = \frac{5^m-1}{9^m-5^m}$; comparing this sequence against the 15 positive rational ratios κ realized on $\mathcal{M}_4$ leaves only $m = -1$ ($\kappa = 9$, 25 squares) and $m = +1$ ($\kappa = 1$, 25 squares). □

2.3 Three-Dimensional Spoke Stars: Unit-Sphere Counterweights and Cubic Vertical Balance

We now lift the spoke sculpture into three dimensions (Figure 3). In 3D, trimming all sixteen spokes to the unit sphere S^2 ($\beta = 0$) breaks equilibrium on 832 of the 880 squares, sparing only the 48 associative squares of Group III where antipodal pairs cancel pairwise ($\hat{\mathbf{p}}_{-c} = -\hat{\mathbf{p}}_c$). Nevertheless, because the natural unequal lengths $R_{ij}(\lambda) > 0$ satisfy $\sum_{i,j} R_{ij}(\lambda)\hat{\mathbf{p}}_{ij}(\lambda) = \mathbf{0}$, the origin O always lies strictly inside the convex hull of the sixteen unit rays, guaranteeing that positive unequal tip weights $\mathbf{w}^* > \mathbf{0}$ restore unit-sphere equilibrium for every magic square.

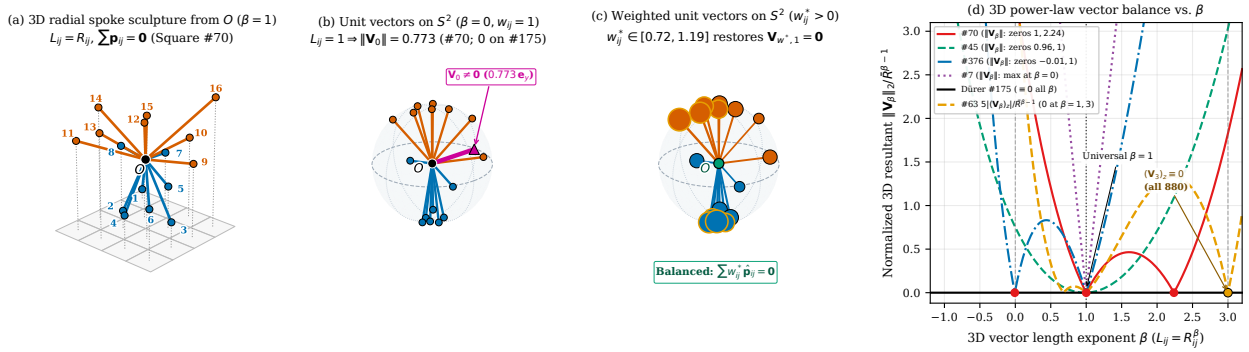


Figure 3: Three-dimensional radial spoke sculptures from the origin $O = (0, 0, 0)$ under variable length and tip weight. (a) Natural 16-spoke sculpture $\mathbf{p}_{ij}$ ($\beta = 1$, orange $z_{ij} > 0$, blue $z_{ij} < 0$) of non-associative square #70, balancing identically at O. (b) Trimming all spokes to the unit sphere S^2 ($\beta = 0$, equal weights) leaves a non-zero resultant $\mathbf{V}_0 = (0, 0.773, 0)$ (magenta arrow) on #70, whereas antipodal pairs cancel on Dürer #175. (c) Minimum-variance positive tip weights $w^*_{ij} \in [0.72, 1.19]$ (gold-rimmed for $w^*_{ij} > 1$) restore exact unit-sphere balance $\sum w^*_{ij}\hat{\mathbf{p}}_{ij} = \mathbf{0}$. (d) Normalized resultant $\|\mathbf{V}_\beta(S; 1)\|_2/\bar{R}^{\beta-1}$ versus exponent β, showing universal balance at $\beta = 1$, second roots $\beta^* \neq 1$ on Group VI squares (#70, #45, #376), and universal vertical vanishing $(\mathbf{V}_3)_z = 0$ at $\beta = 3$ (gold dashed curve).

Theorem 2.5 (3D Power-Law Vectors, Cubic Vertical Vanishing, and Positive Unit-Sphere Weights)**.** *Let S be a semi-magic square of order n and let $\lambda > 0$. For cubic 3D spoke lengths $L_{ij} = R_{ij}(\lambda)^3$ from the origin (dual by Proposition 2.2 to weighting $\mathbf{p}_{ij}(\lambda)$ by $w_{ij} = R_{ij}(\lambda)^2 = r_{ij}^2 + \lambda^2 z_{ij}^2$), the vertical z-component vanishes identically for every semi-magic square of any order n and every $\lambda > 0$:*

$$\mathbf{V}_3(S; \lambda) = \sum_{i,j} (r_{ij}^2 + \lambda^2 z_{ij}^2)(x_j, y_i, \lambda z_{ij}) = \left(\lambda^2 \sum_{i,j} z_{ij}^2 x_j, \quad \lambda^2 \sum_{i,j} z_{ij}^2 y_i, \quad 0 \right), \tag{12}$$

and at order $n = 4$, $\mathbf{V}_3(S; \lambda) = \mathbf{0}$ if and only if S is one of the 48 associative magic squares. Similarly, under any even weight function $w_{ij} = f(|z_{ij}|)$, every associative square satisfies $\hat{\mathbf{p}}_{-c}(\lambda) = -\hat{\mathbf{p}}_c(\lambda)$ and hence $\mathbf{V}_\beta(S; \lambda) = \mathbf{0}$ for all $\beta \in \mathbb{R}$ and $\lambda > 0$; at $n = 4$, $\mathbf{V}_0(S; \lambda) = \mathbf{0}$ holds if and only if S is one of the 48 associative squares ($\|\mathbf{V}_0(S; 1)\|_2 \in [0.0072, 2.4284]$ on the remaining 832 squares), while among the 304 Group VI squares (where C_2 symmetry confines $\mathbf{V}_\beta(S; \lambda)$ to a single coordinate axis), 107 squares possess a second 3D power-law balance exponent $\beta^*(S) \in [-3, 4] \setminus \{1\}$ with $\mathbf{V}_{\beta^*}(S; 1) = \mathbf{0}$ (Figure 3(d)). Finally, letting $\hat{P}(\lambda) \in \mathbb{R}^{N\times 3}$ have rows $\hat{\mathbf{p}}_{ij}(\lambda)^\top$, the unique weight vector $\mathbf{w}^*(S; \lambda)$ of minimum Euclidean distance $\|\mathbf{w} - \mathbf{1}\|_2$ from uniform weights $\mathbf{1}$ satisfying $\sum_{i,j} w^*_{ij}\hat{\mathbf{p}}_{ij}(\lambda) = \mathbf{0}$ is

$$\mathbf{w}^*(S; \lambda) = \mathbf{1} - \hat{P}(\lambda)\big(\hat{P}(\lambda)^\top \hat{P}(\lambda)\big)^{-1}\mathbf{V}_0(S; \lambda), \tag{13}$$

which is strictly positive ($\mathbf{w}^*(S; \lambda) > \mathbf{0}$) across all 880 order-four magic squares at $\lambda = 1$, $\lambda_{\text{iso}} = 1/\sqrt{17}$, and $\lambda_{\text{cube}} = 0.20$ (Figure 3(c)), with $\|\mathbf{w}^*(S; 1) - \mathbf{1}\|_2 \in [0.0052, 1.5967]$ across the 832 non-associative squares.

Proof. Expanding $\mathbf{V}_3(S;\lambda) = \sum_{i,j}(r_{ij}^2 + \lambda^2 z_{ij}^2)(x_j, y_i, \lambda z_{ij})$, the horizontal sum $\sum_{i,j} r_{ij}^2(x_j, y_i)$ vanishes by odd grid symmetry, leaving $\lambda^2 \sum_{i,j} z_{ij}^2(x_j, y_i)$. The vertical component is $\lambda \sum_{i,j}(x_j^2 + y_i^2)z_{ij} + \lambda^3 \sum_{i,j} z_{ij}^3$; here $\sum_{i,j}(x_j^2+y_i^2)z_{ij} = 0$ because $x_j^2+y_i^2 \in W_{\mathrm{rc}}$, and $\sum_{i,j} z_{ij}^3 = 0$ by odd symmetry of $\{z_{ij}\}$, proving (12). For associative squares, $z(-x,-y) = -z(x,y)$ implies $\mathbf{p}_{-c}(\lambda) = -\mathbf{p}_c(\lambda)$ and $R_{-c}(\lambda) = R_c(\lambda)$, so opposite cells cancel pairwise for every $\beta \in \mathbb{R}$. Minimizing $\frac{1}{2}\|\mathbf{w} - \mathbf{1}\|_2^2$ subject to $\hat{P}(\lambda)^\top \mathbf{w} = \mathbf{0}$ by Lagrange multipliers gives (13), and exact enumeration over the 880 squares establishes positivity and the stated bounds. □

Notice how the cubic resultant $\mathbf{V}_3(S;\lambda)$ in (12) bridges static rays and rotational dynamics: while its vertical component vanishes for every semi-magic square, its residual horizontal dipole $\lambda^2 \sum_{i,j} z_{ij}^2(x_j, y_i)$ measures the quadratic height asymmetry across the grid. In Section 3, we set our sculptures into three-dimensional rotation and show that this exact vector governs the vertical off-diagonal products of inertia of an entry-weighted gem.

3 Rotational Dynamics: Smooth Precession and Dzhanibekov Flips

Our second test moves from static radial equilibrium to three-dimensional rotation. Suppose a Magic Gem or radial spoke sculpture of total mass M and centre of mass $\mathbf{c}$ is supported on a low-friction conical pivot or gimbal at the origin O under uniform gravity $\mathbf{g} = (0, 0, -g)^\top$ (generalizing the conical fulcrum of `weighted_ring.stl` in [12]), or tossed in free space. About the pivot O, gravity exerts the torque

$$\boldsymbol{\tau}_{\mathrm{grav}} = M\,\mathbf{c} \times \mathbf{g},$$

which vanishes identically in every 3D orientation if and only if the centre of mass lies at the pivot ($\mathbf{c} = \mathbf{0}$). Consequently, any balanced sculpture ($\mathbf{c} = \mathbf{0}$) supported at O rotates under Earth's gravity according to Euler's exact torque-free equations [2, 10]: in the principal body frame, the angular velocity vector $\boldsymbol{\omega} = (\omega_1, \omega_2, \omega_3)^\top$ evolves via

$$I_1\dot{\omega}_1 = (I_2 - I_3)\omega_2\omega_3, \qquad I_2\dot{\omega}_2 = (I_3 - I_1)\omega_3\omega_1, \qquad I_3\dot{\omega}_3 = (I_1 - I_2)\omega_1\omega_2, \tag{14}$$

where I_1, I_2, I_3 are the principal moments of inertia. For an asymmetric body with three distinct principal moments $I_1 < I_2 < I_3$, rotation about the intermediate axis I_2 is exponentially unstable: any small perturbation grows at rate $\sqrt{(I_2 - I_1)(I_3 - I_2)/(I_1 I_3)}\,|\omega_2|$, causing the body to execute the 180° flips of the Dzhanibekov (or tennis-racket) theorem [3, 15].

When the sixteen unequal heights z_{ij} of a magic square are set spinning in $\mathbb{R}^3$, do their geometric inequalities produce an asymmetric top that tumbles via Dzhanibekov flips, or does line-sum equality enforce smooth axisymmetric precession?

3.1 Equal Masses at Unequal Heights Form a Universal Axisymmetric Rotor

Consider first the discrete point cloud $P_S(\lambda) = \{\mathbf{p}_{ij}(\lambda) = (x_j, y_i, \lambda z_{ij})\}$ carrying equal point masses $m = M/N$ at the $N = n^2$ unequal lifted points (for instance, identical steel bearings mounted at the tips of the sixteen radial spokes $\mathbf{p}_{ij}(\lambda)$ on a lightweight hub at O). Because $\mathbf{c} = \frac{1}{N}\sum_{i,j} \mathbf{p}_{ij}(\lambda) = \mathbf{0}$, gravitational torque about O vanishes identically for every semi-magic square, and the magic line sums neutralize all off-diagonal products of inertia.

Theorem 3.1 (Universal symmetric-top law, spherical-top scale, and periodic polhodes)**.** *Let S be any arrangement of $\{1, \dots, n^2\}$ ($n \geq 2$) whose height field has vanishing first moments $\sum_{i,j} x_j z_{ij} = \sum_{i,j} y_i z_{ij} = 0$ (in particular, any semi-magic or magic square), and place equal point masses $m = M/N$ at the points $\mathbf{p}_{ij}(\lambda) = (x_j, y_i, \lambda z_{ij})$. For every $\lambda > 0$, the inertia tensor about the origin O,*

$$I(\lambda) = \frac{M}{N} \sum_{i,j} \Big(\|\mathbf{p}_{ij}(\lambda)\|_2^2\, I_3 - \mathbf{p}_{ij}(\lambda)\mathbf{p}_{ij}(\lambda)^\top \Big),$$

is diagonal and strictly axisymmetric about the z-axis:

$$I(\lambda) = M\,\mathrm{diag}\big(I_\perp(\lambda),\, I_\perp(\lambda),\, I_{zz}\big), \qquad I_\perp(\lambda) = a_n + \lambda^2 b_n, \qquad I_{zz} = 2a_n, \tag{15}$$

with universal principal inertia ratio

$$\frac{I_\perp(\lambda)}{I_{zz}} = \frac{a_n + \lambda^2 b_n}{2a_n} = \frac{1 + \lambda^2(n^2+1)}{2}. \tag{16}$$

Varying the vertical lift scale λ drives the rotor through three critical aspect ratios (Figure 4(a)). At the canonical lift $\lambda = 1$,

$$\frac{I_\perp(1)}{I_{zz}} = \frac{n^2+2}{2}, \tag{17}$$

which is an exact integer for every even order n (9 for $n = 4$, 19 for $n = 6$, 33 for $n = 8$) and a half-integer for every odd order n (11/2 for $n = 3$, 27/2 for $n = 5$). At the spherical-top critical scale

$$\lambda_{\mathrm{iso}}(n) = \frac{1}{\sqrt{n^2+1}} \qquad \Big(\tfrac{1}{\sqrt{10}} \approx 0.3162 \text{ for } n = 3, \quad \tfrac{1}{\sqrt{17}} \approx 0.2425 \text{ for } n = 4\Big), \tag{18}$$

$I_\perp(\lambda_{\mathrm{iso}}) = I_{zz} = 2a_n$, so $I(\lambda_{\mathrm{iso}}) = 2Ma_nI_3$ is a scalar multiple of the identity and the point-weighted gem is a spherical top *for which every axis through O in $\mathbb{R}^3$ is a principal axis of inertia. At the cubic bounding-box scale $\lambda_{\mathrm{cube}}(n) = \frac{n-1}{n^2-1} = \frac{1}{n+1}$ (where the vertical span matches the horizontal footprint $[-\frac{n-1}{2}, \frac{n-1}{2}]^2$, giving $\lambda_{\mathrm{cube}} = 1/5 = 0.20$ at $n = 4$),*

$$\frac{I_\perp(\lambda_{\mathrm{cube}})}{I_{zz}} = \frac{n^2+n+1}{(n+1)^2} \qquad \Big(\frac{21}{25} = 0.84 \text{ at } n = 4\Big). \tag{19}$$

Because $I_{xx}(\lambda) = I_{yy}(\lambda) = I_\perp(\lambda)$, no distinct intermediate principal axis exists: in torque-free motion (14), $\omega_3(t) = \omega_{3,0}$ is constant and the transverse angular velocity $(\omega_1(t), \omega_2(t))$ precesses in a uniform circle at the body-frame polhode frequency

$$\Omega_{\mathrm{body}}(\lambda) = \frac{I_\perp(\lambda) - I_{zz}}{I_\perp(\lambda)}\,\omega_{3,0} = \frac{\lambda^2(n^2+1) - 1}{\lambda^2(n^2+1) + 1}\,\omega_{3,0}, \tag{20}$$

closing periodically after $(n^2+2)/2 = 9$ spin revolutions at $\lambda = 1$ ($n = 4$) and rotating without wobble ($\Omega_{\mathrm{body}} = 0$) about any initial angular velocity vector $\boldsymbol{\omega}_0 \in \mathbb{R}^3$ at $\lambda = \lambda_{\mathrm{iso}}(n)$.

Proof. By [14, Lem. 3.1], the empirical covariance matrix $\Sigma(\lambda) = \frac{1}{N}\sum_{i,j} \mathbf{p}_{ij}(\lambda)\mathbf{p}_{ij}(\lambda)^\top$ has diagonal entries $\Sigma_{xx} = \Sigma_{yy} = a_n = (n^2-1)/12$ and $\Sigma_{zz} = \lambda^2 b_n = \lambda^2(n^4-1)/12 = \lambda^2(n^2+1)a_n$, while $\Sigma_{xy} = 0$ by grid symmetry and $\Sigma_{xz} = \Sigma_{yz} = 0$ by vanishing of the first moments. Since $I(\lambda) = M\big(\mathrm{tr}(\Sigma(\lambda))I_3 - \Sigma(\lambda)\big)$, we obtain (15) and (16). Evaluating (16) at $\lambda = 1$, $\lambda = (n^2+1)^{-1/2}$, and $\lambda = (n+1)^{-1}$ yields (17)–(19). Substituting $I_1 = I_2 = I_\perp(\lambda)$ and $I_3 = I_{zz}$ into Euler's equations (14) gives $\dot\omega_3 = 0$ and $\dot\omega_1 = \Omega_{\mathrm{body}}\omega_2$, $\dot\omega_2 = -\Omega_{\mathrm{body}}\omega_1$ with Ω_{body} as in (20). □

3.2 Unequal Entry Masses Expose Q_{xy} and Trigger Dzhanibekov Flips

The universal axisymmetric rotation of Theorem 3.1 breaks as soon as each cell is weighted by its *unequal magic entry* $m_{ij} = s_{ij}$, as in the planar balancing wheel `weighted_ring.stl` [12]. While Loly's theorem [11] keeps the diagonal moments equal ($I_{xx} = I_{yy} = I_0$), the unequal masses expose a second-order quadrant inequality—the planar quadrupole moment $Q_{xy}(S) = \sum_{i,j} z_{ij}x_jy_i$—together with the cubic 3D vector resultant $\mathbf{V}_3(S;\lambda)$ from Section 2. On square #46 (Figure 1(d)), for example, the heavy entries $\{16, 13, 15, 14\}$ concentrate in the NW/SE quadrants ($xy < 0$) while the light entries $\{1, 4, 2, 3\}$ sit in the NE/SW quadrants ($xy > 0$). Flicking the board to spin about its intermediate diagonal axis $y = -x$ ($I_2 = 230$) places the angular velocity directly on the saddle of the Poinsot energy ellipsoid (Figure 4(b)), triggering a 180° Dzhanibekov flip (Figure 4(c)).

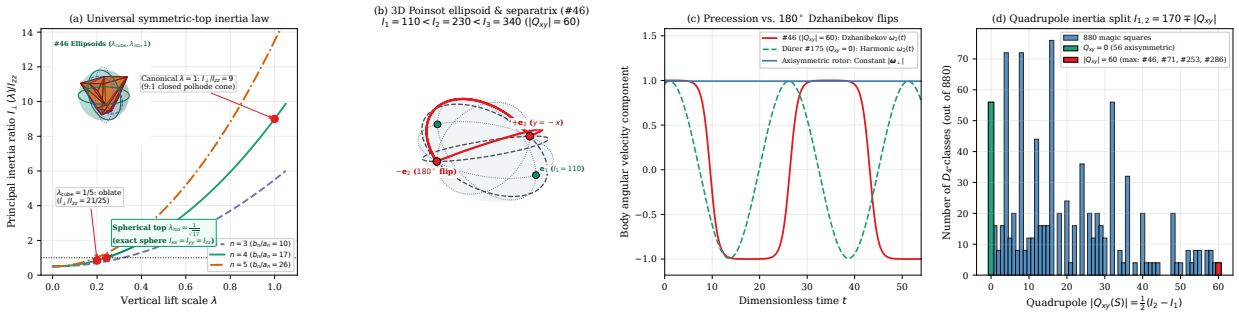


Figure 4: Three-dimensional rotational dynamics of Magic Gems. (a) Universal inertia ratio $I_\perp(\lambda)/I_{zz} = \frac{1}{2}(1+\lambda^2(n^2+1))$ versus vertical scale λ for $n = 3, 4, 5$, with 3D inertia ellipsoids at $\lambda_{\text{cube}} = 1/5$ (21/25), the spherical-top transition $\lambda_{\text{iso}} = 1/\sqrt{17}$ (1), and $\lambda = 1$ (9) for $n = 4$. (b) Triaxial Poinsot energy ellipsoid of entry-weighted square #46 ($I_1 = 110 < I_2 = 230 < I_3 = 340$), showing the figure-eight separatrix and heteroclinic polhode connecting $+\omega_2$ to $-\omega_2$. (c) Euler time series (14): an axisymmetric magic rotor precesses harmonically with constant $|\boldsymbol{\omega}_\perp|$, whereas entry-weighted square #46 ($|Q_{xy}| = 60$) executes periodic 180° Dzhanibekov flips between $+\omega_2$ and $-\omega_2$. (d) Census of the quadrupole split $|Q_{xy}(S)| = \frac{1}{2}(I_2 - I_1)$ across all 880 order-four magic squares.

Theorem 3.2 (Entry-weighted inertia split, quadrupole Dzhanibekov instability, and 3D lifted tensor)**.** *Let S be any semi-magic square of order n, and assign entry masses $m_{ij} = s_{ij} = \bar{s} + z_{ij}$ with total mass $M = \sum_{i,j} s_{ij} = N\bar{s} = n^2(n^2+1)/2$. When the masses $m_{ij} = s_{ij}$ are placed at the planar grid positions $(x_j, y_i, 0) \in \mathbb{R}^3$, the centre of mass lies at O and the 3×3 inertia tensor about O is*

$$I^{(s)}(S) = \begin{pmatrix} I_0 & -Q_{xy}(S) & 0 \\ -Q_{xy}(S) & I_0 & 0 \\ 0 & 0 & 2I_0 \end{pmatrix}, \quad I_0 = Ma_n = \frac{n^2(n^4-1)}{24}, \quad Q_{xy}(S) = \sum_{i,j} z_{ij}x_j y_i, \tag{21}$$

whose principal moments of inertia along the horizontal diagonals $y = \pm x$ and the vertical z-axis are

$$I_1(S) = I_0 - |Q_{xy}(S)|, \qquad I_2(S) = I_0 + |Q_{xy}(S)|, \qquad I_3 = 2I_0. \tag{22}$$

At order $n = 4$ ($I_0 = 170$, $I_3 = 340$), exactly 56 of the 880 magic squares satisfy $Q_{xy}(S) = 0$ (48 associative squares in Group III, including Dürer's #175, plus 8 in Groups IX–X), remaining axisymmetric rotors with $I_1 = I_2 = 170$; the remaining 824 squares have $|Q_{xy}(S)| \in \{1, \ldots, 60\}$ (peaking at $|Q_{xy}| = 60$, $I_1 = 110 < I_2 = 230 < I_3 = 340$, on Group VI squares #46, #71, #253, and #286) and undergo unstable Dzhanibekov flips about $y = -\operatorname{sgn}(Q_{xy})\, x$ at dimensionless exponential growth rate

$$\Gamma(S) = \sqrt{\frac{(I_2 - I_1)(I_3 - I_2)}{I_1 I_3}} = \sqrt{\frac{|Q_{xy}(S)|}{I_0}} = \sqrt{\frac{|Q_{xy}(S)|}{170}}.$$

When the entry masses $m_{ij} = s_{ij} = \bar{s} + z_{ij}$ are placed at the 3D lifted points $\mathbf{p}_{ij}(\lambda) = (x_j, y_i, \lambda z_{ij})$ ($\lambda > 0$), larger entries $s_{ij} > \bar{s}$ sit at positive heights $z_{ij} > 0$ while smaller entries $s_{ij} < \bar{s}$ sit at negative heights $z_{ij} < 0$, biasing the vertical moment upward by $\lambda \sum_{i,j} z_{ij}^2$ and shifting the centre of mass to $\mathbf{c}^{(s)}(\lambda) = (0, 0, z_{\text{cm}}(\lambda))$ with $z_{\text{cm}}(\lambda) = \lambda b_n/\bar{s} = \frac{\lambda(n^2-1)}{6}$ ($= \frac{5}{2}\lambda$ at $n = 4$). Because $\sum_{i,j} z_{ij}^3 = 0$, the diagonal moments of inertia about O are $I^{(s)}_{xx,O}(\lambda) = I^{(s)}_{yy,O}(\lambda) = M(a_n + \lambda^2 b_n)$ and $I^{(s)}_{zz,O}(\lambda) = 2I_0$, matching the equal-mass gem in Theorem 3.1. Translating to the true centre of mass $\mathbf{c}^{(s)}(\lambda)$ via Steiner's parallel-axis theorem leaves $I^{(s)}_{zz,\text{cm}} = 2I_0$ and all off-diagonal products unchanged while subtracting $Mz_{\text{cm}}(\lambda)^2$ from the horizontal diagonal moments, giving

$$I^{(s)}_{xx,\text{cm}}(\lambda) = I^{(s)}_{yy,\text{cm}}(\lambda) = M\left(a_n + \lambda^2 b_n\left(1 - \frac{b_n}{\bar{s}^2}\right)\right) = Ma_n\left(1 + \frac{2(n^2+2)}{3}\lambda^2\right)$$

$(= 170(1+12\lambda^2)$ *at* $n=4$*). In both frames (*O *and* $\mathbf{c}^{(s)}(\lambda)$*), the off-diagonal products of inertia are* $I_{xy}^{(s)} = -Q_{xy}(S)$ *and*

$$\big(I_{xz}^{(s)}(\lambda),\, I_{yz}^{(s)}(\lambda)\big) = -\lambda \sum_{i,j} z_{ij}^2 (x_j, y_i) = -\lambda^{-1}\Big(\big(\mathbf{V}_3(S;\lambda)\big)_x,\, \big(\mathbf{V}_3(S;\lambda)\big)_y\Big),$$

so an order-four magic square has a diagonal, axisymmetric 3D entry-weighted inertia tensor if and only if it is one of the 48 *associative squares (*$Q_{xy}=0$ *and* $\mathbf{V}_3 = \mathbf{0}$*).*

Proof. Since every row excess $R_i = \sum_j z_{ij}$ and column excess $C_j = \sum_i z_{ij}$ vanishes, $\sum_{i,j} s_{ij} x_j^2 = \bar{s}\sum_{i,j} x_j^2 + \sum_j x_j^2 C_j = Ma_n = I_0$ and $\sum_{i,j} s_{ij} y_i^2 = I_0$, giving $I_{xx} = I_{yy} = I_0$ and $I_{zz} = 2I_0$. Since $\sum_{i,j} x_j y_i = 0$, $I_{xy} = -\sum_{i,j} s_{ij} x_j y_i = -Q_{xy}(S)$. Diagonalizing $\left(\begin{smallmatrix} I_0 & -Q_{xy} \\ -Q_{xy} & I_0 \end{smallmatrix}\right)$ yields eigenvalues $I_0 \mp |Q_{xy}|$ along $(1,\pm 1)/\sqrt{2}$, proving (21)–(22). At $n=4$, $I_0 = 170$, $|Q_{xy}| \le 60 < 170$, and $I_3 - I_2 = 2I_0 - (I_0 + |Q_{xy}|) = I_1$ simplifies $\sqrt{(I_2-I_1)(I_3-I_2)/(I_1 I_3)}$ to $\sqrt{|Q_{xy}|/I_0}$.

At the 3D lifted points $\mathbf{p}_{ij}(\lambda)$, $\sum_{i,j} s_{ij}(x_j, y_i) = \mathbf{0}$ while $\sum_{i,j}(\bar{s}+z_{ij})\lambda z_{ij} = \lambda \sum_{i,j} z_{ij}^2 = N\lambda b_n$, giving $z_{\mathrm{cm}}(\lambda) = \lambda b_n/\bar{s}$. Since $\sum_{i,j} z_{ij}^3 = 0$, $\sum_{i,j}(\bar{s}+z_{ij})\lambda^2 z_{ij}^2 = M\lambda^2 b_n$, so $I_{xx,O}^{(s)}(\lambda) = I_{yy,O}^{(s)}(\lambda) = M(a_n + \lambda^2 b_n)$. Steiner's theorem subtracts $Mz_{\mathrm{cm}}(\lambda)^2\,\mathrm{diag}(1,1,0)$, and $1 - b_n/\bar{s}^2 = \frac{2(n^2+2)}{3(n^2+1)}$ gives $b_n(1 - b_n/\bar{s}^2) = \frac{2(n^2+2)}{3} a_n$. Finally, $I_{xz}^{(s)}(\lambda) = -\lambda\sum_{i,j} z_{ij}^2 x_j = -\lambda^{-1}(\mathbf{V}_3)_x$ and similarly for $I_{yz}^{(s)}(\lambda)$, both of which vanish alongside $Q_{xy}(S)$ on all 48 associative squares by Theorem 2.5. □

3.3 From Point Clouds to Continuous Polyhedra: Why Solid Hulls Tilt on the Pivot

What happens to rotational stability when we replace the discrete point cloud P_S by the uniform-density 3D solid polyhedron $\mathcal{G}_0(S) = \mathrm{conv}\, P_S$? Decomposing $\mathcal{G}_0(S)$ into exact rational tetrahedra (Section A) shows that about its own centre of mass $\mathbf{c}_0(S)$, the solid inertia tensor remains remarkably close to the axisymmetric point-mass rotor of Theorem 3.1: across all 880 squares at $\lambda = 1$, the ratio of the mean transverse moment $\frac{1}{2}(I_2 + I_3)$ to the axial moment I_1 averages 9.41 (ranging over [7.34, 11.57], tracking the point-mass value 9), and the relative transverse splitting between I_2 and I_3 remains below 2.5% ($\frac{I_3 - I_2}{I_2} \in [0.00004, 0.0243]$, mean 0.0071).

Yet when we place the cast solid $\mathcal{G}_0(S)$ on our pivot at the grid origin O under gravity, a more basic failure occurs: on 829 of the 880 squares, taking the convex hull shifts the solid centre of mass $\mathbf{c}_0(S)$ off the origin ($\mathbf{c}_0(S) \neq \mathbf{0}$), so gravity immediately exerts a tipping torque $\boldsymbol{\tau}_{\mathrm{grav}} = M\mathbf{c}_0(S) \times \mathbf{g} \neq \mathbf{0}$. Understanding why the convex hull breaks centroid balance—and how the interior points of the magic square restore it—is the subject of Section 4.

4 Convex Hulls and "Diamond-in-a-Diamond" Counterweighting

Why does passing from the discrete point cloud P_S ($\sum_{i,j} \mathbf{p}_{ij} = \mathbf{0}$) to its uniform-density solid convex hull $\mathcal{G}_0(S) := \mathcal{G}(S) = \mathrm{conv}\, P_S$ shift the solid centre of mass

$$\mathbf{c}_0(S) := \mathbf{c}_{\mathrm{solid}}(\mathcal{G}_0(S)) = \frac{1}{\mathrm{vol}\,\mathcal{G}_0(S)} \iiint_{\mathcal{G}_0(S)} \mathbf{x}\, dV$$

away from the origin O on 829 of the 880 order-four magic squares? Taking the three-dimensional convex hull introduces two geometric inequalities: first, the boundary $\partial\mathcal{G}_0(S)$ depends solely on the $V_0 = |\,\mathrm{vert}\,\mathcal{G}_0(S)|$ extreme vertices and omits the $V_1 = N - V_0$ interior and non-vertex points $P_S^{(1)} = P_S \setminus \mathrm{vert}\,\mathcal{G}_0(S)$; second, even when $V_0 = N = 16$ (18 of the 880 squares), decomposing $\mathcal{G}_0(S)$ into tetrahedra from O weights each simplex Δ_k by its volume $\mathrm{vol}(\Delta_k)$ rather than weighting the sixteen vertices equally.

Since the outer hull vertices and the discarded inner points together sum to zero, their centroids must pull in strictly opposite directions across O. We now test whether physically re-engaging the inner core $\mathcal{G}_1(S) = \mathrm{conv}\, P_S^{(1)}$ restores exact balance at O across cast solids, 3D-printed wireframes, complete strut networks, and folded papercraft shells.

4.1 The 51 Naturally Balanced Solids and Outer–Inner Vertex Opposition

We first classify the 51 order-four magic squares whose uniform solid hull $\mathcal{G}_0(S)$ balances at O without any counterweight, and then prove the outer–inner opposition law for the remaining 829 squares.

Proposition 4.1 (Classification of the 51 naturally balanced order-four gems)**.** *Across the* 880 *magic squares of order* 4*, the uniform solid* $\mathcal{G}_0(S)$ *has centre of mass* $\mathbf{c}_0(S) = \mathbf{0}$ *for exactly* 51 *squares, consisting of the* 48 *associative squares (Dudeney's Group III, where* $z(-x,-y) = -z(x,y)$ *implies* $\mathcal{G}_0(S) = -\mathcal{G}_0(S)$ *and forces* $\mathbf{c}_0(S) = -\mathbf{c}_0(S) = \mathbf{0}$ *by central inversion) together with three non-associative squares in Dudeney's Group VI: squares #86, #739, and #756 (Table 1).*

Proof. For every associative square S, $P_S = -P_S$ implies $\mathcal{G}_0(S) = -\mathcal{G}_0(S)$ and $\mathbf{c}_0(S) = \mathbf{0}$. Each of the three Group VI squares #86, #739, and #756 satisfies $\overline{S} = hS$ or $\overline{S} = vS$, so $\mathcal{G}_0(S)$ is invariant under a 180° half-turn $\iota_h\colon (x,y,z) \mapsto (x,-y,-z)$ or $\iota_v\colon (x,y,z) \mapsto (-x,y,-z)$ in $\mathbb{R}^3$ [14, Prop. 4.3]. The half-turn forces two coordinates of $\mathbf{c}_0(S)$ to vanish identically, and exact simplicial integration (Section A) certifies that the single remaining rational axial moment vanishes exclusively on #86, #739, and #756 among all 832 non-associative squares. □

Table 1: The three non-associative order-four magic squares whose uniform solid $\mathcal{G}_0(S)$ has exact centre of mass $\mathbf{c}_0(S) = \mathbf{0}$, together with their inner core $\mathcal{G}_1(S) = \operatorname{conv}(P_S \setminus \operatorname{vert}\mathcal{G}_0(S))$. All three squares lie in Dudeney's Group VI and have 12 outer vertices and 4 inner points (spanning a planar parallelogram in #86 and a 3D tetrahedron in #739 and #756) whose centroid $\mathbf{c}_1(S)$ is also $\mathbf{0}$.

Gem	Dudeney	$f(\mathcal{G}_0)$	$\operatorname{vol}(\mathcal{G}_0)$	$\operatorname{Iso}(\mathcal{G}_0)$	$\dim$ / $\operatorname{vol}(\mathcal{G}_1)$	First row of standard form S
#86	Group VI	$(12, 28, 18)$	209/3	C_2 $(\overline{S} = vS)$	2D (0)	$(1, 7, 14, 12)$
#739	Group VI	$(12, 26, 16)$	287/3	C_2 $(\overline{S} = hS)$	3D (5/3)	$(4, 14, 3, 13)$
#756	Group VI	$(12, 24, 14)$	84	C_2 $(\overline{S} = hS)$	3D (4/3)	$(5, 2, 15, 12)$

To counter the centroid drift on the remaining 829 squares, we peel P_S into nested convex layers [4]:

$$P_S^{(0)} = P_S, \qquad \mathcal{G}_k(S) = \operatorname{conv} P_S^{(k)}, \qquad P_S^{(k+1)} = P_S^{(k)} \setminus \operatorname{vert}\mathcal{G}_k(S) \quad (k \geq 0), \tag{23}$$

calling $\mathcal{G}_0(S)$ the *outer gem* and $\mathcal{G}_1(S) = \operatorname{conv} P_S^{(1)} \subset \mathcal{G}_0(S)$ the *inner core gem*—"a diamond inside a diamond" (Figure 5(a,b)).

Proposition 4.2 (Vertex-centroid opposition and order-four onion hierarchy)**.** *Let* S *be any arrangement of order* n *with* $V_0 = |\operatorname{vert}\mathcal{G}_0(S)| < N$ *and* $V_1 = N - V_0$*. The centroid* $\overline{\mathbf{p}}_{\text{outer}} = \frac{1}{V_0}\sum_{\mathbf{p}\in\operatorname{vert}\mathcal{G}_0}\mathbf{p}$ *of the outer hull vertices and the centroid* $\overline{\mathbf{p}}_{\text{inner}} = \frac{1}{V_1}\sum_{\mathbf{p}\in P_S^{(1)}}\mathbf{p}$ *of the inner core points satisfy*

$$V_0\,\overline{\mathbf{p}}_{\text{outer}} + V_1\,\overline{\mathbf{p}}_{\text{inner}} = \mathbf{0}, \tag{24}$$

pointing in strictly opposite directions across O *whenever* $\overline{\mathbf{p}}_{\text{outer}} \neq \mathbf{0}$*. Across the* 880 *magic squares of order* 4 *(Figure 5(c)),* 18 *squares have* $V_0 = 16$ *(*$P_S^{(1)} = \emptyset$*),* 842 *squares have onion depth* 2 *(*14 *singletons,* 162 *segments,* 175 *planar polygons, and* 491 *3D polyhedra* $\mathcal{G}_1(S)$*), and* 20 *squares have onion depth* 3 *(*$\mathcal{G}_0 \supset \mathcal{G}_1 \supset \mathcal{G}_2$*, comprising* 16 *with dimension sequence* $(3,3,0)$ *and* 4 *with* $(3,3,1)$*), so in total* 511 *order-four magic squares possess a three-dimensional inner core gem* $\mathcal{G}_1(S)$*.*

Proof. Equation (24) follows immediately from $\sum_{\mathbf{p}\in P_S}\mathbf{p} = \mathbf{0}$ and $P_S = \operatorname{vert}\mathcal{G}_0(S) \sqcup P_S^{(1)}$, and exact convex-hull peeling across all 880 squares yields the stated layer census. □

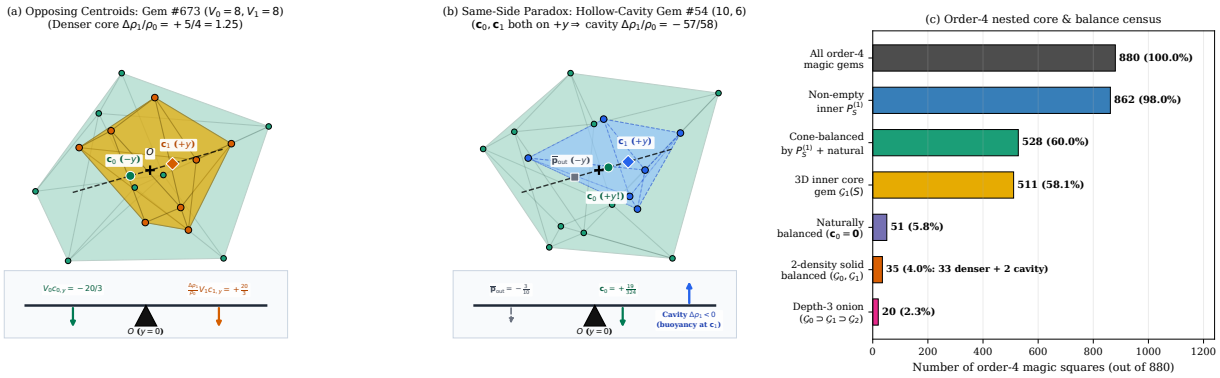


Figure 5: Nested "diamond-in-a-diamond" convex layers $\mathcal{G}_0(S) \supset \mathcal{G}_1(S)$ and centre-of-mass restoration. (a) Denser-core Gem #673 ($(V_0, V_1) = (8, 8)$) and (b) hollow-cavity Gem #54 ($(V_0, V_1) = (10, 6)$, 1-swap sibling of #45), showing the translucent outer hull $\mathcal{G}_0(S)$ around the inner core $\mathcal{G}_1(S)$ with 2D fulcrum lever diagrams below. On #673, $\mathbf{c}_0$ (green circle) and $\mathbf{c}_1$ (gold diamond) lie on opposite sides of O, balancing via a heavier inner core ($\Delta\rho_1/\rho_0 = +5/4$). On #54, volumetric simplex weighting pulls $\mathbf{c}_0 = (0, 19/324, 0)$ onto the $+y$ side alongside $\mathbf{c}_1 = (0, 29/68, 0)$, so a 98.3% hollow core cavity ($\Delta\rho_1/\rho_0 = -57/58$) restores balance at O. (c) Census of nested layer dimensions and solid balance mechanisms across all 880 order-four magic squares.

4.2 Restoring Solid Balance via "Diamond-in-a-Diamond" Core Inclusions

Guided by the opposition identity (24), our first restoration method plays the inner core $\mathcal{G}_1(S)$ directly against the outer solid hull $\mathcal{G}_0(S)$. For a two-density composite solid to balance via a single scalar density increment $\Delta\rho_1$, the 3D vectors $\mathbf{c}_0(S)$ and $\mathbf{c}_1(S)$ must be collinear—which occurs in Dudeney's Group VI, where C_2 half-turn symmetry locks both centroids onto the same coordinate axis.

Theorem 4.3 (Composite "diamond-in-a-diamond" solid balancing)**.** *Let S be an order-four magic square with $\dim \mathcal{G}_1(S) = 3$ (511 squares), and fabricate $\mathcal{G}_0(S)$ with baseline density $\rho_0 > 0$ and inner core inclusion $\mathcal{G}_1(S) \subset \mathcal{G}_0(S)$ of excess density $\Delta\rho_1 = \rho_1 - \rho_0$. The composite centre of mass*

$$\mathbf{c}_{\text{comp}} = \frac{\rho_0 \operatorname{vol}(\mathcal{G}_0)\, \mathbf{c}_0 + \Delta\rho_1 \operatorname{vol}(\mathcal{G}_1)\, \mathbf{c}_1}{\rho_0 \operatorname{vol}(\mathcal{G}_0) + \Delta\rho_1 \operatorname{vol}(\mathcal{G}_1)}$$

vanishes for some $\Delta\rho_1 \neq 0$ if and only if $\mathbf{c}_0$ and $\mathbf{c}_1$ are non-zero and collinear ($\mathbf{c}_0 \times \mathbf{c}_1 = \mathbf{0}$), with unique balancing density increment

$$\frac{\Delta\rho_1}{\rho_0} = -\frac{\operatorname{vol}(\mathcal{G}_0)\,(\mathbf{c}_0 \cdot \mathbf{c}_1)}{\operatorname{vol}(\mathcal{G}_1)\,\|\mathbf{c}_1\|_2^2}. \tag{25}$$

Across the 511 order-four gems with $\dim \mathcal{G}_1(S) = 3$, 207 gems have $\mathbf{c}_1 = \mathbf{0}$ (13 associative gems plus 194 non-associative gems whose four inner points form a zero-sum tetrahedron) and 254 gems outside Group VI have non-collinear solid centroids $\mathbf{c}_0 \times \mathbf{c}_1 \neq \mathbf{0}$. Among the remaining 50 gems (all in Dudeney's Group VI), 33 have strictly anti-parallel solid centroids ($\mathbf{c}_0 \cdot \mathbf{c}_1 < 0$), balanced by a denser inner core with rational excess density $\Delta\rho_1/\rho_0 \in [5/4, 191/6]$ (Table 2 and Table 5), led by Gem #673 at $\Delta\rho_1/\rho_0 = 5/4$ (Figure 1(e), Figure 5(a)); the other 17 have parallel solid centroids pointing in the same direction ($\mathbf{c}_0 \cdot \mathbf{c}_1 > 0$), because volumetric simplex weighting pulls $\mathbf{c}_0$ onto the same side of O as $\mathbf{c}_1$ despite the opposite vertex centroids of (24), and two of these 17 gems balance with non-negative core density $\rho_1 \in [0, \rho_0)$: square #123 ($\Delta\rho_1/\rho_0 = -3/17$, $\rho_1/\rho_0 = 14/17$, a lighter core) and square #54 ($\Delta\rho_1/\rho_0 = -57/58$, $\rho_1/\rho_0 = 1/58$, a nearly hollow core cavity, Figure 5(b)), which differs from denser-core square #45 ($\Delta\rho_1/\rho_0 = +85/61$) by the single border swap $(8, 9) \leftrightarrow (15, 2)$ (Figure 1(c)).

More generally, placing non-negative point masses $m_q \geq 0$ at the inner points $q \in P_S^{(1)}$ balances the uniform solid $\mathcal{G}_0(S)$ at O if and only if $-\mathbf{c}_0(S) \in \operatorname{cone}(P_S^{(1)})$, which holds for 477 of the 829

unbalanced gems ($528/880 = 60.0\%$ *including the* 51 *naturally balanced solids), while partitioning* $\mathcal{G}_0(S)$ *into* N *cells of equal mass* M/N *with centroids at* $\mathbf{p}_{ij}$ *(or embedding* N *identical dense beads at* $\mathbf{p}_{ij}$ *in a lightweight shell) yields* $\mathbf{c}_{\mathrm{comp}} = \mathbf{0}$ *and restores the axisymmetric inertia tensor of Theorem 3.1 for every semi-magic square of any order* n*.*

Proof. Setting $\rho_0 \operatorname{vol}(\mathcal{G}_0)\mathbf{c}_0 + \Delta\rho_1 \operatorname{vol}(\mathcal{G}_1)\mathbf{c}_1 = \mathbf{0}$ and evaluating the exact rational simplicial moments (Section A) across all 511 gems with $\dim \mathcal{G}_1(S) = 3$ yields (25) and the four-class partition. Existence of non-negative inner point masses $m_q \geq 0$ is equivalent to $-\mathbf{c}_0 \in \operatorname{cone}(P_S^{(1)})$ and certified by linear programming over the 829 unbalanced gems, while the bead-inlaid identity follows directly from $\sum_{i,j} \mathbf{p}_{ij} = \mathbf{0}$ and Theorem 3.1. □

Table 2: The eight order-four Magic Gems with the smallest balancing excess density ratios $\Delta\rho_1/\rho_0 \in [5/4, 40/19] \approx [1.25, 2.11]$ in a two-density "diamond-in-a-diamond" solid inclusion $(\mathcal{G}_0(S), \mathcal{G}_1(S))$ (Theorem 4.3), all achievable with standard dual-material 3D printing. All 33 denser-core gems belong to Dudeney's Group VI; the full list of 33 is given in Table 5.

Gem	(V_0, V_1)	$\operatorname{vol}(\mathcal{G}_0)$	$\operatorname{vol}(\mathcal{G}_1)$	Axial c_0	Axial c_1	Exact $\Delta\rho_1/\rho_0$	Decimal ρ_1/ρ_0
#673	$(8, 8)$	$257/3$	$56/3$	$-20/257$	$+2/7$	$5/4$	2.250
#502	$(10, 6)$	$271/3$	6	$+2/271$	$-1/12$	$4/3$	2.333
#45	$(10, 6)$	$214/3$	6	$-85/856$	$+61/72$	$85/61$	2.393
#50	$(10, 6)$	$254/3$	$22/3$	$-7/127$	$+19/44$	$28/19$	2.474
#307	$(10, 6)$	$277/3$	$22/3$	$+23/1108$	$-15/88$	$23/15$	2.533
#49	$(12, 4)$	81	2	$-2/81$	$+1/2$	2	3.000
#38	$(10, 6)$	$263/3$	$22/3$	$+31/1052$	$-15/88$	$31/15$	3.067
#47	$(10, 6)$	$247/3$	$22/3$	$-20/247$	$+19/44$	$40/19$	3.105

4.3 Overcoming the Density Barrier: Complete K_N Networks, Nested Wireframes, and Papercraft Shells

While the eight gems in Table 2 have modest excess density ratios $\Delta\rho_1/\rho_0 \in [5/4, 40/19]$ that print directly on a dual-extruder 3D printer (such as standard PLA around a tungsten- or bronze-filled PLA core), the remaining 25 denser-core gems in Table 5 have small core volumes $\operatorname{vol}(\mathcal{G}_1)$ requiring $\Delta\rho_1/\rho_0 \in [47/12, 191/6]$, and 194 gems have a four-vertex tetrahedral core whose solid centroid $\mathbf{c}_{\mathrm{solid}}(\mathcal{G}_1) = \frac{1}{4}\sum \mathbf{p}_q = \mathbf{0}$ provides no lever arm at all.

Replacing solid volume with the skeletal and thin-shell architectures of `magicGemWeb` [12] (Figure 6) overcomes both barriers. Connecting all $\binom{N}{2}$ pairs of points as a complete strut network $K_N\big(P_S(\lambda)\big)$ (`magicGem_v2.stl`, Figure 6(b)) restores equal participation of all N vertices; building a nested ball-and-rod wireframe $G(\mathcal{G}_0) \cup G(\mathcal{G}_1)$ (`magicGem_v1.stl`, Figure 6(a)) replaces volumetric scaling with quadratic rod-diameter scaling ($\rho_{\mathrm{lin}} \propto d^2$) and gives four-vertex tetrahedral cores a non-zero edge-length centroid $\mathbf{c}_{\mathrm{wire}}(\mathcal{G}_1) \neq \mathbf{0}$; and unfolding $\partial\mathcal{G}_\lambda(S)$ along a dual spanning tree produces a flat printable papercraft net (Figure 6(c)).

Theorem 4.4 (Complete K_N strut networks and two-gauge nested wireframes)**.** *Let* S *be an arrangement of* $\{1, \ldots, N\}$*,* $N = n^2$ *(*$n \geq 2$*), with* $\sum_{u=1}^{N} \mathbf{p}_u(\lambda) = \mathbf{0}$ *and empirical covariance matrix* $\Sigma(\lambda) = \frac{1}{N}\sum_{u=1}^{N} \mathbf{p}_u(\lambda)\mathbf{p}_u(\lambda)^\top$ *in the slender-rod limit* $d/L_{uv} \to 0^+$*. If each of the* $\binom{N}{2}$ *rods connecting* $\mathbf{p}_u(\lambda)$ *and* $\mathbf{p}_v(\lambda)$ *(*$1 \leq u < v \leq N$*) carries equal mass* $m_{\mathrm{edge}} = M_{\mathrm{rods}}/\binom{N}{2}$ *(with optional equal node masses* $m_{\mathrm{node}} = M_{\mathrm{nodes}}/N$*), then* $(N-1)$*-regularity of* K_N *places the centre of mass at* O *for every arrangement* S*:*

$$\mathbf{c}\big(K_N(\lambda)\big) = \frac{1}{\binom{N}{2}} \sum_{1 \leq u < v \leq N} \frac{\mathbf{p}_u(\lambda) + \mathbf{p}_v(\lambda)}{2} = \frac{1}{N}\sum_{u=1}^{N} \mathbf{p}_u(\lambda) = \mathbf{0}, \tag{26}$$

and the continuous second-moment covariance matrix of the $\binom{N}{2}$ rods is a universal scalar multiple of $\Sigma(\lambda)$:

$$\Sigma_{\text{rods}}^{(=mass)}\big(K_N(\lambda)\big) = \frac{2N-3}{3(N-1)}\,\Sigma(\lambda) \qquad \Big(= \frac{5}{8}\,\Sigma(\lambda) \text{ at } n=3, \quad \frac{29}{45}\,\Sigma(\lambda) \text{ at } n=4\Big), \tag{27}$$

so that for every semi-magic square S, the equal-mass complete network $K_N\big(P_S(\lambda)\big)$ shares the exact axisymmetric inertia ratio $I_\perp(\lambda)/I_{zz} = \frac{1}{2}\big(1+\lambda^2(n^2+1)\big)$ and spherical-top scale $\lambda_{\text{iso}} = (n^2+1)^{-1/2}$ of Theorem 3.1.

When a subgraph $G=(V_G,E_G)$ is instead printed with uniform rod diameter d so that each rod has mass proportional to its length $L_{uv}(\lambda) = \|\mathbf{p}_u(\lambda) - \mathbf{p}_v(\lambda)\|_2$, both K_{16} and the outer wireframe $G(\mathcal{G}_0)$ have $\mathbf{c}_{\text{len}} = \mathbf{0}$ if and only if S is one of the 48 associative squares, while passing from $G(\mathcal{G}_0)$ to the 120-rod complete network K_{16} reduces mean centroid drift $\|\mathbf{c}_{\text{len}}\|_2$ across $\mathcal{M}_4$ by 2.7× at $\lambda=1$ (from 0.194 to 0.072) and by 3.6× at $\lambda=0.20$ (from 0.088 to 0.025; Figure 6(d)). Furthermore, for the 848 order-four gems with $\dim \mathcal{G}_1(S) \geq 1$, printing the outer edges $E(\mathcal{G}_0)$ with rod diameter d_0 and the disjoint inner core edges $E(\mathcal{G}_1)$ with rod diameter d_1 restores $\mathbf{c}_{\text{wire}}(\mathcal{G}_0 \cup \mathcal{G}_1) = \mathbf{0}$ whenever $\mathbf{c}_{\text{wire}}(\mathcal{G}_0)$ and $\mathbf{c}_{\text{wire}}(\mathcal{G}_1)$ are strictly anti-parallel, at the unique rod diameter ratio

$$\frac{d_1}{d_0} = \sqrt{\frac{\rho_{\text{lin},1}}{\rho_{\text{lin},0}}} = \sqrt{-\frac{L\big(G(\mathcal{G}_0)\big)\,\big(\mathbf{c}_{\text{wire}}(\mathcal{G}_0)\cdot\mathbf{c}_{\text{wire}}(\mathcal{G}_1)\big)}{L\big(G(\mathcal{G}_1)\big)\,\|\mathbf{c}_{\text{wire}}(\mathcal{G}_1)\|_2^2}}, \tag{28}$$

balancing 158 Group VI gems at $\lambda=1$ (such as Gem #673 at $d_1/d_0 = 0.793$ and Gem #45 at $d_1/d_0 = 0.795$) and 164 Group VI gems at $\lambda = 0.20$.

Proof. Integrating $\mathbf{x}(t) = (1-t)\mathbf{p}_u + t\mathbf{p}_v$ over $t\in[0,1]$ gives midpoint $\frac{1}{2}(\mathbf{p}_u+\mathbf{p}_v)$ and second moment $\frac{1}{3}(\mathbf{p}_u\mathbf{p}_u^\top + \mathbf{p}_v\mathbf{p}_v^\top) + \frac{1}{6}(\mathbf{p}_u\mathbf{p}_v^\top + \mathbf{p}_v\mathbf{p}_u^\top)$. Since each vertex belongs to $N-1$ edges of K_N and $\sum_{u<v}(\mathbf{p}_u\mathbf{p}_v^\top + \mathbf{p}_v\mathbf{p}_u^\top) = -N\Sigma(\lambda)$, averaging over $\binom{N}{2}$ edges yields (26)–(27). Exact evaluation of the edge lengths and (28) across all 880 squares establishes the length-weighted and nested wireframe censuses (Section A). □

Proposition 4.5 (Papercraft cutout nets, glue-tab invariant, and nested thin-shell balance)**.** *Let $\mathcal{G}_\lambda(S)$ be any three-dimensional Magic Gem with f-vector (f_0,f_1,f_2). Unfolding $\partial\mathcal{G}_\lambda(S)$ into a connected planar net along any spanning tree T^* of the dual facet graph $G^*(\mathcal{G})$ [7, 18, 5, 9] partitions the f_1 edges into f_2-1 interior fold creases and $N_{\text{tabs}} = f_1-(f_2-1)$ cut edges joined by trapezoidal glue tabs (paired by labels* `a`*–*`k` *in Figure 6(c)). Because $\partial\mathcal{G}_\lambda(S)\cong S^2$, the cut edges $E\setminus E(T^*)$ form a spanning tree T of the primal 1-skeleton $G(\mathcal{G}_\lambda)$ on the f_0 hull vertices, so the number of glue tabs depends solely on the hull vertex count f_0:*

$$N_{\text{tabs}} = f_1 - (f_2-1) = |E(T)| = f_0 - 1, \tag{29}$$

taking every integer value in $\{7,\dots,15\}$ across $\mathcal{M}_4$ (11 tabs for Dürer's #175). Under the deterministic breadth-first dual spanning tree T^* rooted at the largest-area facet F_0 (★F_0 in Figure 6(c)), all 880 order-four Magic Gems (100%) unfold into strictly non-overlapping 2D planar nets at both $\lambda=1$ and $\lambda=0.20$. Moreover, a uniform boundary shell $\partial\mathcal{G}_\lambda(S)$ of areal density $\sigma_0>0$ has $\mathbf{c}_{\text{shell}}(\mathcal{G}_0)=\mathbf{0}$ on the 48 associative squares, and enclosing a nested inner shell $\partial\mathcal{G}_1(S)$ ($\dim\mathcal{G}_1=3$) of areal density σ_1 restores $\mathbf{c}_{\text{shell}}(\partial\mathcal{G}_0\cup\partial\mathcal{G}_1)=\mathbf{0}$ for 80 Group VI gems at $\lambda=1$ (87 at $\lambda=0.20$).

Proof. By planar graph duality on $\partial\mathcal{G}_\lambda(S)\cong S^2$, the complement of a dual spanning tree $T^*\subset G^*(\mathcal{G}_\lambda)$ ($|E(T^*)| = f_2-1$) is a primal spanning tree $T\subset G(\mathcal{G}_\lambda)$ on the f_0 vertices, giving $N_{\text{tabs}} = |E(T)| = f_0-1$ (invariant under facet triangulation). Exact 2D polygon intersection testing and triangular surface moments certify non-overlap and the shell censuses across all 880 gems (Section A). □

Remark 4.6 (Physical realization of finite-diameter struts and core suspension). In a physical 3D print of finite rod diameter $d>0$, each cylindrical strut of length L_{uv} and direction $\hat{\mathbf{e}}_{uv}$ retains

midpoint centroid $\frac{1}{2}(\mathbf{p}_u+\mathbf{p}_v)$ and adds the radial inertia correction $m_{uv}\frac{d^2}{16}(I_3+\hat{\mathbf{e}}_{uv}\hat{\mathbf{e}}_{uv}^\top)$ up to $O(d^3)$ hub-overlap volumes. Suspending the inner core wireframe $G(\mathcal{G}_1)$ inside $G(\mathcal{G}_0)$ on a Group VI gem via C_2-symmetric pairs of equal-length struts places the suspension centroid at O, leaving the balancing diameter ratio d_1/d_0 in (28) invariant.

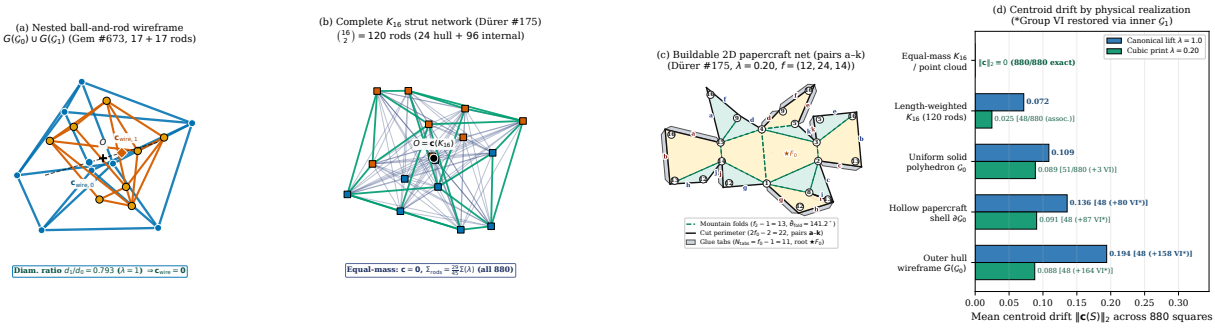


Figure 6: Wireframes, complete K_{16} strut networks, and unfolded papercraft cutout nets of Magic Gems [12]. (a) Nested ball-and-rod wireframe $G(\mathcal{G}_0)\cup G(\mathcal{G}_1)$ of Gem #673 (17 outer blue rods and 17 inner orange rods), balanced at rod-diameter ratio $d_1/d_0 = 0.793$ ($\lambda = 1$). (b) Complete network K_{16} of Dürer's Gem #175 with all $\binom{16}{2} = 120$ rods (24 hull edges in green, 96 internal cross-struts in slate), which satisfies $\mathbf{c}(K_{16}) = \mathbf{0}$ and $\Sigma_{\text{rods}} = \frac{29}{45}\Sigma(\lambda)$ for equal-mass rods across all 880 squares. (c) Exact 2D unfolded papercraft net of Dürer's Gem #175 ($\lambda = 0.20$, $f = (12, 24, 14)$) rooted at $\bigstar F_0$, with $f_2 - 1 = 13$ dashed fold creases and $N_{\text{tabs}} = f_0 - 1 = 11$ glue tabs paired by labels a–k. (d) Mean centroid drift $\|\mathbf{c}(S)\|_2$ across all 880 squares for the five physical realizations at $\lambda = 1.0$ and $\lambda = 0.20$.

Having restored internal balance to individual polyhedra, we now remove the central pivot O in Section 5 and place Magic Gems directly on a flat horizontal table and into multi-block vertical stacks under gravity.

5 Freestanding Gravity and Mirror-Twin Towers

Our fourth and final test removes the central pivot and places Magic Gems directly onto a flat horizontal table under gravity—first as individual resting blocks, and then stacked face-to-face into multi-block vertical columns. Because the hull vertices sit at unequal heights, the boundary facets of $\mathcal{G}_\lambda(S)$ are slanted polygons whose outward normals rarely oppose each other across the gem. We therefore test when a slanted facet $F \subset \partial\mathcal{G}_\lambda(S)$ supports the gem's centre of mass without tipping, and how pairing a gem with an inverted partner restores a straight vertical column when identical copies curve off-axis.

5.1 Single-Block Table Equilibrium: Cubic Aspect Scaling Stabilizes 74.5% of Facets

Let $F \subset \partial\mathcal{G}_\lambda(S)$ be a facet with outward unit normal $\hat{\mathbf{n}}_F(\lambda)$. When $\mathcal{G}_\lambda(S)$ rests with F on a horizontal table (so $\hat{\mathbf{n}}_F(\lambda)$ points straight down), gravity acts vertically through the centre of mass $\mathbf{c}(\lambda)$. Let $\pi_F(\mathbf{c}(\lambda))$ denote the orthogonal projection of $\mathbf{c}(\lambda)$ onto the affine plane of F, and let $h_F(\lambda) = (\mathbf{p}_F - \mathbf{c}(\lambda)) \cdot (-\hat{\mathbf{n}}_F(\lambda)) > 0$ be the height of the centre of mass above the table.

Definition 5.1 (Static stability margin and critical tipping angle)**.** For a facet $F \subset \partial\mathcal{G}_\lambda(S)$, the *stability margin* $d_{\text{stab}}(S, F; \lambda)$ is the signed Euclidean distance in the plane of F from $\pi_F(\mathbf{c}(\lambda))$ to the boundary ∂F of the facet polygon (positive when $\pi_F(\mathbf{c}(\lambda))$ lies in the strict relative interior of F, and negative outside). Facet F is *statically stable* if and only if $d_{\text{stab}}(S, F; \lambda) > 0$, with *critical tipping angle*

$$\theta_{\text{tip}}(S, F; \lambda) = \arctan\left(\frac{d_{\text{stab}}(S, F; \lambda)}{h_F(\lambda)}\right). \tag{30}$$

Proposition 5.2 (Order-four resting stability census)**.** *Across all* 880 *magic squares of order* 4*, the gems* $\mathcal{G}_\lambda(S)$ *possess a total of* 14,824 *facets (mean* 16.85 *facets per gem). At the tall canonical lift* $\lambda = 1$ *(where the vertical height span* 15 *is five times the* 3×3 *floor span), the high centre of mass* $\mathbf{c}_0(S)$ *projects outside* 57.0% *of all facet polygons:* 6,378 *of the* 14,824 *facets (*43.0%*) are statically stable, with every gem possessing between* 4 *and* 12 *stable resting facets (mean* 7.25*; using the balanced point centroid* O *gives* 6,340 *stable facets,* 42.8%*). Compressing the vertical lift to the cubic 3D-print scale* $\lambda_{\text{cube}} = 1/5 = 0.20$ *brings the centre of mass closer to the slanted upper and lower facets so that* 11,044 *of the* 14,824 *facets (*74.5%*) become statically stable, with a mean critical tipping angle of* 17.8° *and a maximum of* 47.3° *(Figure 7(d)).*

Proof. For each facet $F \subset \partial\mathcal{G}_\lambda(S)$ with exact integer plane equation $aX + bY + cZ + d = 0$ in doubled coordinates, rescaling $z \mapsto \lambda z$ transforms the outward normal to $\mathbf{n}_F(\lambda) \propto (a\lambda, b\lambda, c)$ and the solid centroid to $\mathbf{c}_0(\lambda) = (c_{0,x}, c_{0,y}, \lambda c_{0,z})$. Projecting $\mathbf{c}_0(\lambda)$ onto the plane of F and evaluating $d_{\text{stab}}(S, F; \lambda)$ and (30) across all 14,824 facets yields the stated counts and angles. □

5.2 Why Same-Gem Stacks Wedge Apart, and How Mirror-Twin Inversion Restores Verticality

Suppose we now stack multiple blocks vertically along an upper facet $F_+ \subset \mathcal{G}_\lambda(S)$ (outward normal $+\mathbf{n}_+$, $n_{+,z} > 0$) and a lower facet $F_- \subset \mathcal{G}_\lambda(S)$ (outward normal $+\mathbf{n}_-$, $n_{-,z} < 0$). Stacking translated copies of the *same* gem $\mathcal{G}_\lambda(S)$ without rotation requires parallel opposite normals $\mathbf{n}_- = -\mathbf{n}_+$, which fails on 756 of the 880 gems (85.9%); when $\mathbf{n}_- \neq -\mathbf{n}_+$, identical copies meet at an open wedge angle that bends the column away from the vertical (Figure 7(c), left).

Equilibrium is restored by pairing a gem with its *rotational complement (mirror twin)*

$$S^* := r^2\overline{S} = (N+1)\mathbf{1} - r^2 S, \tag{31}$$

which inverts the polyhedron through the origin in $\mathbb{R}^3$ and pairs every slanted upper facet with an equal and opposite lower facet (Figure 7(a,c)).

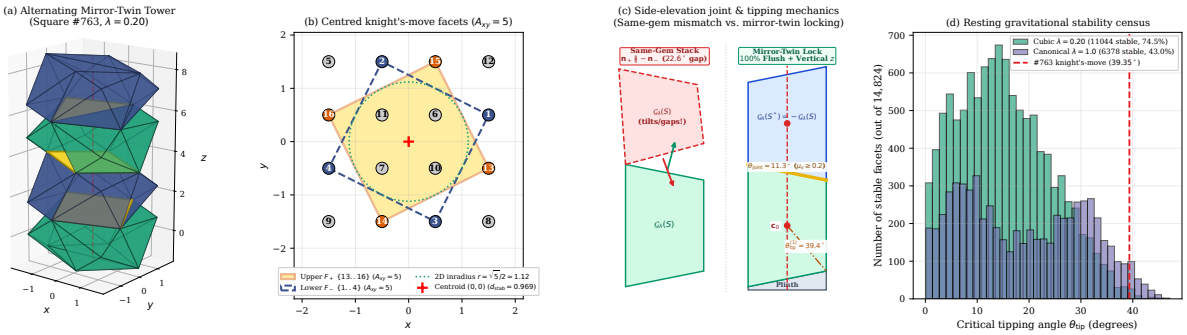


Figure 7: Mirror-twin facet locking and periodic vertical towers. (a) Four-block alternating tower of square #763 at $\lambda = 0.20$, alternating $\mathcal{G}_\lambda(S)$ (green) with its mirror twin $\mathcal{G}_\lambda(r^2\overline{S}) = -\mathcal{G}_\lambda(S)$ (blue) along the golden knight's-move contact facets $\{13, 14, 15, 16\}$ and $\{1, 2, 3, 4\}$ to keep the column's centre of mass on the z-axis (red dashed). (b) Top-down (x, y) footprint of square #763 showing the dual knight's-move squares of area $A_{xy} = 5$ and 2D inradius $r = \sqrt{5}/2 \approx 1.12$ ($d_{\text{stab}} = 0.969$ in the tilted plane at $\lambda = 0.20$). (c) Side-elevation schematic comparing the $2\theta_{\text{joint}} = 22.6°$ wedge mismatch of same-gem stacking against flush mirror-twin locking ($\mathbf{n}_+^* = -\mathbf{n}_+$) on an 11.3° base plinth. (d) Census of critical tipping angles θ_{tip} over all 14,824 facets at $\lambda = 0.20$ and $\lambda = 1.0$.

Theorem 5.3 (Mirror-Twin Inversion and Zero-Rotation Alternating Towers)**.** *Let* S *be any arrangement of order* n*, let* $S^* = r^2\overline{S}$ *be its half-turned complement, and let* $\lambda > 0$*. In* $\mathbb{R}^3$*, the lifted point clouds and convex hulls satisfy the central inversion identity*

$$P_{S^*}(\lambda) = -P_S(\lambda), \qquad \mathcal{G}_\lambda(S^*) = -\mathcal{G}_\lambda(S), \tag{32}$$

so the map $F \mapsto F^* := -F$ is an area-preserving, normal-reversing bijection between the upper facets $F_+ \subset \mathcal{G}_\lambda(S)$ (outward normal $+\mathbf{n}_+$) and the lower facets $F_+^* \subset \mathcal{G}_\lambda(S^*)$ (outward normal $-\mathbf{n}_+$), and between the lower facets $F_- \subset \mathcal{G}_\lambda(S)$ (outward normal $+\mathbf{n}_-$) and the upper facets $F_-^* = -F_- \subset \mathcal{G}_\lambda(S^*)$ (outward normal $-\mathbf{n}_-$).

Consequently, given any upper facet $F_+ \subset \mathcal{G}_\lambda(S)$ and any lower facet $F_- \subset \mathcal{G}_\lambda(S)$ (not necessarily parallel) that are centrally symmetric polygons in $\mathbb{R}^3$ with centroids $\mathbf{c}(F_+)$ and $\mathbf{c}(F_-)$, the alternating sequence of unrotated blocks $B_0, B_1, B_2, \ldots$ defined by

$$B_{2m} = \mathcal{G}_\lambda(S) + m\mathbf{T}, \qquad B_{2m+1} = -\mathcal{G}_\lambda(S) + 2\mathbf{c}(F_+) + m\mathbf{T}, \qquad \mathbf{T} = 2\big(\mathbf{c}(F_+) - \mathbf{c}(F_-)\big), \tag{33}$$

meets with 100% polygon and vertex overlap at every odd joint $B_{2m} \cap B_{2m+1}$ (where the upper facet $F_+ + m\mathbf{T}$ of B_{2m} coincides identically with the lower facet $-F_+ + 2\mathbf{c}(F_+) + m\mathbf{T}$ of B_{2m+1} with opposite outward normals $\pm\mathbf{n}_+$) and at every even joint $B_{2m-1} \cap B_{2m}$ (where the upper facet $-F_- + 2\mathbf{c}(F_+) + (m-1)\mathbf{T}$ of B_{2m-1} coincides identically with the lower facet $F_- + m\mathbf{T}$ of B_{2m} with opposite outward normals $\mp\mathbf{n}_-$). Every two-block repeating unit $B_{2m} \cup B_{2m+1}$ is centrally symmetric about $\mathbf{c}(F_+) + m\mathbf{T}$, and whenever $\mathbf{c}(F_+) = (0, 0, z_+)$ and $\mathbf{c}(F_-) = (0, 0, z_-)$ both lie on the vertical z-axis ($z_+ > 0 > z_-$), the period vector $\mathbf{T} = (0, 0, 2(z_+ - z_-))$ is purely vertical and places the centre of mass of any $2M$-block tower on the z-axis regardless of whether $\mathbf{c}_0(S) = \mathbf{0}$ (Figure 7(a,c)).

Proof. In centred coordinates (1), r^2 sends $(x, y) \mapsto (-x, -y)$ and complementation sends $z \mapsto -z$, so $r^2\overline{S}$ lifts to $-\mathbf{p}_{ij}(\lambda)$, proving (32). Central symmetry of $F_\pm$ about $\mathbf{c}(F_\pm)$ gives $-F_\pm + 2\mathbf{c}(F_\pm) = F_\pm$; translating by $m\mathbf{T}$ establishes identical facet coincidence at all odd and even joints, while central inversion about $\mathbf{c}(F_+) + m\mathbf{T}$ exchanges B_{2m} and B_{2m+1} and locks the two-block centroid onto the z-axis. □

5.3 Chiral Knight's-Move Towers: Exemplar Square #763

Proposition 5.4 (Vertically centered tower census and the knight's-move square #763)**.** *Across the 880 magic squares of order 4, exactly 48 squares possess both an upper facet F_+ and a lower facet F_- that are centrally symmetric polygons whose centroids lie on the vertical axis $(0, 0, z_\pm)$. The maximum projected horizontal contact area among these 48 squares is $A_{xy} = 5$ (spanning $5/9 \approx 55.6\%$ of the 3×3 grid footprint), achieved by 17 squares (Table 3; e.g. squares #603, #763, and #774) in which $\pi_{xy}(F_+)$ is the centred 2×1 knight's-move square with vertices $(\pm\frac{3}{2}, \mp\frac{1}{2})$ and $(\pm\frac{1}{2}, \pm\frac{3}{2})$ (Figure 7(b)). Only two of the 17 (#774 and #792) have parallel top and bottom facets ($\mathbf{n}_- = -\mathbf{n}_+$); the remaining 15 require mirror-twin alternation.*

In particular, square #763 (Dudeney Group VI, $\overline{S} = hS$, so $S^* = r^2\overline{S} = vS$ is its vertical reflection) is obtained from naturally balanced solid #756 ($\mathbf{c}_0 = \mathbf{0}$, Table 1) by swapping the single complementary pair $(4, 13) \leftrightarrow (16, 1)$ in rows 2–3 (Figure 1(f)):

$$S_{\#763} = \begin{pmatrix} 5 & 2 & \mathbf{15} & 12 \\ \mathbf{16} & 11 & 6 & 1 \\ 4 & 7 & 10 & \mathbf{13} \\ 9 & \mathbf{14} & 3 & 8 \end{pmatrix}, \qquad S^*_{\#763} = vS_{\#763} = \begin{pmatrix} 9 & 14 & 3 & 8 \\ 4 & 7 & 10 & 13 \\ 16 & 11 & 6 & 1 \\ 5 & 2 & 15 & 12 \end{pmatrix}.$$

This swap lifts $\{13, 14, 15, 16\}$ onto the Pythagorean upper knight's-move plane $4x - 3y + 5z = 30$ (centroid $(0, 0, 6\lambda)$) and $\{1, 2, 3, 4\}$ onto the lower plane $-4x - 3y - 5z = 30$ (centroid $(0, 0, -6\lambda)$), while shifting the solid centroid slightly to $\mathbf{c}_0 = (0, -5/126, 0)$ (which cancels pairwise in $B_{2m} \cup B_{2m+1}$). Both facets have 3D area $5\sqrt{1+\lambda^2}$, stability margin $d_{\text{stab}} = 0.969$, and single-block tipping angle $\theta_{\text{tip}}^{(1)} = 39.35°$ at $\lambda = 0.20$. Because $\mathbf{n}_\pm(\lambda) \propto (\pm 4\lambda, -3\lambda, \pm 5)$ makes angle $\theta_{\text{joint}}(\lambda) = \arctan(\lambda)$ with $\hat{\mathbf{e}}_z$ ($\approx 11.31°$ at $\lambda = 0.20$), any material with static friction $\mu_s > \lambda = 0.20$ holds the unbonded column at level ($\theta_{\text{table}} = 0$), while tilting an M-block column of centre-of-mass height H_M is governed by $\min\big(\arctan(\mu_s) - \theta_{\text{joint}}(\lambda), \arctan(d_{\text{stab}}/H_M)\big)$ (Figure 7(c)).

Proof. Testing each facet $F \subset \partial\mathcal{G}_1(S)$ across the 880 gems for central symmetry ($F = 2\mathbf{c}(F) - F$ with $c_x(F) = c_y(F) = 0$) identifies the 48 gems and the 17 gems of projected shoelace area $A_{xy} = 5$. Substituting the lifted coordinates of $\{13, 14, 15, 16\}$ and $\{1, 2, 3, 4\}$ on #763 into $4x-3y+5(z/\lambda) = 30$ and $-4x-3y-5(z/\lambda) = 30$ verifies the facet planes, normals $\mathbf{n}_\pm(\lambda) \propto (\pm 4\lambda, -3\lambda, \pm 5)$, surface area $5\sqrt{1+\lambda^2}$, and joint tilt $\tan\theta_{\text{joint}}(\lambda) = \lambda$. □

Remark 5.5 (Three-dimensional chirality and why a single mold cannot build the #763 tower). Because square #763 satisfies $\overline{S} = hS$ ($z(-x, y) = -z(x, y)$), its 3D gem $\mathcal{G}_\lambda(S_{\#763})$ is invariant under the 180° proper rotation around the y-axis, $R_{y,\pi}(x, y, z) = (-x, y, -z) \in SO(3)$, which exchanges F_+: $4x - 3y + 5z = 30$ and F_-: $-4x - 3y - 5z = 30$ and returns the exact same block in its original orientation. Flipping a second copy of $\mathcal{G}_\lambda(S_{\#763})$ upside-down around the x-axis via $R_{x,\pi}(x, y, z) = (x, -y, -z)$ maps F_+ to a lower facet with outward normal $(+4\lambda, +3\lambda, -5) \neq -\mathbf{n}_+ = (-4\lambda, +3\lambda, -5)$, failing to mate flush with F_+. More fundamentally, $\text{Aut}_{O(3)}\big(\mathcal{G}_\lambda(S_{\#763})\big) = \{I_3, R_{y,\pi}\} \cong C_2 \subset SO(3)$ contains no improper reflections: $\mathcal{G}_\lambda(S_{\#763})$ and $\mathcal{G}_\lambda(S^*_{\#763}) = -\mathcal{G}_\lambda(S_{\#763})$ are *chiral 3D enantiomorphs* in disjoint proper rigid-motion orbits, so building the tower of Figure 7(a) requires two opposite-handed molds.

Table 3: Representative order-four Magic Gems from the 17 classes (#603, #763, #768, #774, #779, #785, #788, #791, #792, #818, #824, #828, #836, #837, #839, #842, #844) achieving the maximum projected contact area $A_{xy} = 5$ via centred knight's-move square facets F_+ and F_- (Proposition 5.4). Plane equations (a, b, c, d) are given in doubled coordinates $aX + bY + cZ + d = 0$. "Same-gem ∥" indicates whether $\mathbf{n}_- = -\mathbf{n}_+$; stability margins d_{stab} and single-block critical tipping angles $\theta^{(1)}_{\text{tip}}$ (Definition 5.1) are reported for the upper facet at $\lambda = 0.20$.

Gem	Group	Upper F_+ plane	Lower F_- plane	Same-gem ∥	d_{stab} ($\lambda = 0.2$)	$\theta^{(1)}_{\text{tip}}$ ($\lambda = 0.2$)
#603	VI	$(2, -9, 5, -50)$	$(-2, -9, -5, -50)$	No	1.020	45.39°
#763	VI	$(4, -3, 5, -60)$	$(-4, -3, -5, -60)$	No	0.969	39.35°
#768	II	$(0, -1, 1, -12)$	$(-4, -3, -5, -60)$	No	0.973	39.24°
#774	VI	$(1, 0, 1, -12)$	$(-1, 0, -1, -12)$	Yes	0.931	38.35°
#791	VI	$(-3, -4, 5, -60)$	$(-3, 4, -5, -60)$	No	0.969	39.35°
#792	VI	$(0, -1, 1, -12)$	$(0, 1, -1, -12)$	Yes	0.931	38.35°
#837	VI	$(4, -3, 5, -60)$	$(4, 3, -5, -60)$	No	0.962	38.94°

6 Synthesis and Open Questions

Stepping back from the individual theorems, the mechanical tests of Sections 2–5 tell a unified story about how combinatorial *balance in inequality* behaves when lifted from a flat grid of numbers into three-dimensional physical space (Table 4). Across all four physical regimes—radial spokes, spinning rotors, convex polyhedra, and stacked columns—the 880 order-four magic squares stratify into three distinct mechanical tiers determined by how their symmetries interact with nonlinearity.

At the broadest level, whenever a physical observable is linear or symmetric-quadratic in the coordinates (x_j, y_i, z_{ij}), the row and column sum constraints neutralize entry inequality universally across all 880 squares (100%). This universal tier encompasses natural 3D and 2D spoke balance ($\beta = 1, \alpha = 1$), cubic vertical spoke vanishing ($(\mathbf{V}_3)_z = 0$), existence of positive unit-sphere counterweights ($\mathbf{w}^* > \mathbf{0}$), axisymmetric precession and the $\lambda_{\text{iso}} = 1/\sqrt{17}$ spherical-top transition for equal point masses and equal-mass K_{16} strut networks, outer–inner vertex opposition ($V_0\overline{\mathbf{p}}_{\text{outer}} = -V_1\overline{\mathbf{p}}_{\text{inner}}$), non-overlapping papercraft nets with $N_{\text{tabs}} = f_0 - 1$ glue tabs, and mirror-twin facet inversion ($\mathcal{G}_\lambda(r^2\overline{S}) = -\mathcal{G}_\lambda(S)$).

When a nonlinear geometric operation breaks this universal balance, it typically creates a three-component residual imbalance vector $\mathbf{c} = (c_x, c_y, c_z) \in \mathbb{R}^3$ that a single scalar parameter cannot zero out. In Dudeney's Group VI (304 squares satisfying $\overline{S} = hS$ or vS), however, the 180° proper half-turn symmetry ($C_2 \subset SO(3)$) forces two coordinates of every residual vector to vanish identically, locking opposing components onto a single coordinate axis. This axial alignment explains why

one-parameter restoration occurs throughout Group VI: the eight planar Pell-minimum squares (#70, $v/u = 9/4 \approx \sqrt{5}$), the integer power-law spoke roots ($\alpha^* = -1$ on #45 and $\alpha^* = +3$ on #286), all 107 3D power-law spoke roots $\beta^* \neq 1$, the three non-associative balanced solids (#86, #739, #756), all 35 two-density "diamond-in-a-diamond" solids (33 denser cores led by #673 plus the two lighter/hollow-cavity cores #123 and #54), all 158 balanced nested wireframes (d_1/d_0), all 80 balanced nested shells (σ_1/σ_0), and the chiral knight's-move mirror-twin towers (#763).

Finally, when a nonlinear observable requires unweighted equilibrium without an opposing parameter—such as equal-weight unit-sphere spokes ($\mathbf{V}_0 = \mathbf{0}$), full 3D cubic spoke vanishing ($\mathbf{V}_3 = \mathbf{0}$), 3D entry-weighted rotational axisymmetry ($Q_{xy} = 0$ and $\mathbf{V}_3 = \mathbf{0}$), or uniform-diameter wireframes and hollow shells—balance holds if and only if central inversion $\mathbf{p}_{-c}(\lambda) = -\mathbf{p}_c(\lambda)$ cancels opposite cells pairwise, singling out the 48 associative squares of Dudeney's Group III ($r^2 S = \overline{S}$) led by Dürer's #175.

Table 4: Synthesis of the four progressive mechanical tests across the 880 order-four magic squares, organized by Baseline Equilibrium, Nonlinear Symmetry Breaking, and Dual Restoration (certified in exact rational arithmetic; see Section A).

Mechanical Regime	$n = 4$ Count	Universal Law, Breakdown, or Restoration Threshold	Flagship Exemplars
1. Radial Spokes from the Origin (Section 2)			
Linear 3D & 2D spokes ($\beta = 1, \alpha = 1$)	880/880 (100%)	Baseline: $\sum \mathbf{p}_{ij}(\lambda) = \mathbf{0}$, $\mathbf{B}_{z,r} = \mathbf{0}$ identically	All semi-magic
Planar unit spokes ($\alpha = 0$, $r_2/r_1 = \sqrt{5}$)	0/880 vanish	Breakdown: $\min \lVert\mathbf{B}_{\text{unit}}\rVert_2 = \frac{18\sqrt{10}}{5} - 8\sqrt{2} \approx 0.0705$ ($v/u = 9/4$)	8 in VI (#70, #76, …)
Planar power-law restoration ($\ell = r^{\alpha^*}$)	204/880 (23.2%)	Parallel ring dipoles $\mathbf{d}_{\text{out}} = \kappa \mathbf{d}_{\text{in}}$ (25 at $\alpha^* = -1$, 25 at $+3$)	#45 (-1), #286 ($+3$)
3D unit sphere $\sum \hat{\mathbf{p}}_{ij}(\lambda) = \mathbf{0}$ ($\beta = 0$)	48/880 (5.5%)	Pointwise antipodal cancellation ($\iff$ Group III); 107 VI have $\beta^* \neq 1$	#175 (**0**), #70 ($\beta^* \approx 2.24$)
3D unit-sphere tip weights $\mathbf{w}^* > \mathbf{0}$	880/880 (100%)	Restoration: $\sum w_{ij}^* \hat{\mathbf{p}}_{ij} = \mathbf{0}$, $\lVert\mathbf{w}^* - \mathbf{1}\rVert_2 \in [0.005, 1.60]$	All 880 squares
3D cubic spoke law ($\beta = 3$, $L_{ij} = R_{ij}^3$)	880/880 (100%)	Universal vertical vanishing $(\mathbf{V}_3)_z = 0$; $\mathbf{V}_3 = \mathbf{0}$ $\iff$ Group III (48)	All semi-magic ($z = 0$)
2. Rotational Dynamics (Section 3)			
Equal-mass point rotor $I_\perp(\lambda)/I_{zz}$	880/880 (100%)	Baseline: $\frac{1+17\lambda^2}{2}$ (spherical top 1 at $\lambda = \frac{1}{\sqrt{17}}$, prolate 9 at $\lambda = 1$)	All semi-magic
Entry-weighted ($m_{ij} = s_{ij}$) Dzhanibekov split	824/880 flip	Breakdown: $I_{1,2} = 170 \mp \lvert Q_{xy}\rvert$ (56 have $Q_{xy} = 0$; 48 Group III in 3D)	#46 ($\lvert Q_{xy}\rvert = 60$), #175 (0)
3. Convex Hulls, Skeletons, and Shells (Section 4)			
Uniform solid hull $\mathcal{G}_0(S)$ ($\mathbf{c}_0 = \mathbf{0}$)	51/880 (5.8%)	Breakdown on 829 gems; 48 Group III +3 Group VI balance naturally	#175, #86, #739, #756
Outer–inner vertex opposition	862/880 ($V_0 < 16$)	Restoration law: $V_0 \overline{\mathbf{p}}_{\text{outer}} + V_1 \overline{\mathbf{p}}_{\text{inner}} = \mathbf{0}$ (511 have 3D core $\mathcal{G}_1$)	All $V_0 < 16$ gems
Two-density solid ($\mathcal{G}_0, \mathcal{G}_1$)	35/511 3D cores	Group VI: 33 denser (8 with $\Delta\rho_1/\rho_0 \leq \frac{40}{19}$) +2 lighter/hollow cavity	#673 ($\frac{5}{4}$), #45↔#54
Non-negative inner-core point weights	528/880 (60.0%)	51 natural +477 with $-\mathbf{c}_0 \in \text{cone}(P_S^{(1)})$; bead inlay balances 880/880	528 magic gems
Complete K_{16} strut network (120 rods)	880/880 (= mass)	$\mathbf{c} = \mathbf{0}$, $\Sigma_{\text{rods}} = \frac{29}{45}\Sigma(\lambda)$; uniform-diam. drift cut 3.6× at $\lambda = 0.20$	All 880 (#175)
Two-gauge nested wireframe $G(\mathcal{G}_0) \cup G(\mathcal{G}_1)$	206/880 ($\lambda = 1$)	48 Group III +158 Group VI (164 at $\lambda = 0.20$) via rod ratio d_1/d_0	#673 ($d_1/d_0 = 0.793$)
Papercraft nets & nested shells $\partial\mathcal{G}_0$	880/880 nets	100% non-overlapping, $N_{\text{tabs}} = f_0 - 1 \in [7, 15]$; $48 + 80$ VI shells balance	#175 (11 tabs, 13 folds)
4. Freestanding Gravity and Mirror-Twin Towers (Section 5)			
Single-block facet resting stability	11,044/14,824	Cubic aspect $\lambda = 0.20$ raises stability from 43.0% ($\lambda = 1$) to 74.5%	$\max \theta_{\text{tip}} = 47.3°$
Mirror-twin vertical towers $\mathcal{G}_\lambda(r^2\overline{S})$	48/880 (5.5%)	Central inversion $-\mathcal{G}_\lambda(S)$ locks slanted facets (17 area-5 knight's-move)	#763↔#756, #603

These findings suggest several natural directions for further investigation. In the planar spoke regime, the twenty-four non-central cells of A_5 at order $n = 5$ lie on five concentric rings of radii $r \in \{1, \sqrt{2}, 2, \sqrt{5}, 2\sqrt{2}\}$, coupling the independent square-free radicals $\sqrt{2}$ and $\sqrt{5}$; it remains open whether the unit-spoke resultant $\mathbf{B}_{\text{unit}}(S) = \sum z_{ij}\mathbf{u}_{ij}$ can ever vanish at order $n \geq 5$, or how rapidly $\min_{S \in \mathcal{M}_n} \lVert\mathbf{B}_{\text{unit}}(S)\rVert_2$ decays as $n \to \infty$ via simultaneous Diophantine approximation. In the rotational and solid regimes, while point-weighted Magic Gems become exact spherical tops ($I_{xx} = I_{yy} = I_{zz}$) at $\lambda_{\text{iso}} = (n^2+1)^{-1/2}$, the uniform polyhedral solid $\mathcal{G}_\lambda(S)$ retains a small transverse splitting $(I_3 - I_2)/I_2 \in [0.00004, 0.0243]$ at $n = 4$, raising the question of whether a magic square of some order $n \geq 5$ (or a two-density composite $(\mathcal{G}_0, \mathcal{G}_1)$ at $n = 4$) has a continuous solid inertia tensor that is an exact scalar multiple of the identity I_3. In the convex-peeling regime, the outer hull $\mathcal{G}_0(S_n)$ of the Siamese magic square of odd order $n \geq 5$ strips off only twelve vertices [14, Thm. 6.4], leaving $n^2 - 12$ points on five sheared planar polygons whose asymptotic onion-peeling depth $d_{\text{onion}}(S_n)$ and inner layer f-vectors remain to be determined. Finally, beyond vertical mirror-twin columns (Theorem 5.3), it is natural to ask whether a Magic Gem $\mathcal{G}_\lambda(S)$ and its $D_4 \times \langle\tau\rangle$ images can tile a horizontal slab or interlock in three-dimensional space with full facet-to-facet contact.

Acknowledgments

This work grew out of the author's physical and computational explorations of 3D-printed Magic Gems, ball-and-rod wireframes, and folded papercraft models [12], and forms the third part of a series alongside [14, 13]. Large language models (OpenAI's ChatGPT, Anthropic's Claude, and

Google's Gemini) were used by the author as interactive assistants for symbolic checks, verification scripting, interactive simulator prototyping, and manuscript copy-editing; all mathematical formulations, proofs, and exact computational certificates were verified by the author, who takes full responsibility for the work.

References

[1] W. S. Andrews. *Magic Squares and Cubes*. Dover Publications, 2nd edition, 1960.

[2] Vladimir I. Arnold. *Mathematical Methods of Classical Mechanics*, volume 60 of *Graduate Texts in Mathematics*. Springer, New York, 2nd edition, 1989.

[3] Mark S. Ashbaugh, Carmen C. Chicone, and Richard H. Cushman. The twisting tennis racket. *Journal of Dynamics and Differential Equations*, 3(1):67–85, 1991.

[4] Bernard Chazelle. On the convex layers of a planar set. *IEEE Transactions on Information Theory*, 31(4):509–517, 1985.

[5] Erik D. Demaine and Joseph O'Rourke. *Geometric Folding Algorithms: Linkages, Origami, Polyhedra*. Cambridge University Press, Cambridge, 2007.

[6] Henry E. Dudeney. *Amusements in Mathematics*. Thomas Nelson and Sons, London, 1917.

[7] Albrecht Dürer. *Underweysung der Messung, mit dem Zirckel und Richtscheyt, in Linien, Ebnen unnd gantzen Corporen*. Hieronymus Andreae, Nuremberg, 1525.

[8] Bernard Frénicle de Bessy. Des quarrez ou tables magiques. In *Divers ouvrages de mathématique et de physique, par Messieurs de l'Académie Royale des Sciences*. Imprimerie Royale, Paris, 1693.

[9] Mohammad Ghomi. Dürer's conjecture on unfoldings of convex polyhedra. *Proceedings of the American Mathematical Society*, 142(11):3975–3985, 2014.

[10] Herbert Goldstein, Charles P. Poole, and John L. Safko. *Classical Mechanics*. Addison-Wesley, San Francisco, 3rd edition, 2002.

[11] Peter D. Loly. The invariance of the moment of inertia of magic squares. *The Mathematical Gazette*, 88(511):151–153, 2004. Note 88.30.

[12] Kyle Elliott Mathewson. `magicGemWeb`: Interactive 3D-printable ball-and-rod wireframes, complete K_{16} strut networks, and unfolded papercraft cutout nets for magic gems. https://kylemath.github.io/magicGem/3dModels/index.html and https://github.com/kylemath/magicGemWeb, 2025.

[13] Kyle Elliott Mathewson. Bivariate polynomial moments and Prouhet–Tarry–Escott identities of semi-magic squares, 2026. Companion paper II, arXiv preprint.

[14] Kyle Elliott Mathewson. Magic gems: Convex hulls of lifted magic squares. *arXiv preprint arXiv:2512.09170*, 2026. Companion paper I.

[15] Louis Poinsot. *Théorie nouvelle de la rotation des corps*. Bachelier, Paris, 1834.

[16] Adam Rogers and Peter D. Loly. The inertia tensor of a magic cube. *American Journal of Physics*, 72(6):786–789, 2004.

[17] Adam Rogers and Peter D. Loly. The electric multipole expansion for a magic cube. *European Journal of Physics*, 26(5):809–813, 2005.

[18] G. C. Shephard. Convex polytopes with convex nets. *Mathematical Proceedings of the Cambridge Philosophical Society*, 78(3):389–403, 1975.

A Exact computational methods and certificates

All computations in this paper use Python 3.9 with NumPy 2.0, SciPy 1.13, and Python's exact rational module `fractions.Fraction`. The complete verification script `anc/verify_paper_c.py` and figure generator `anc/make_figures_c.py` run in under 10 s on a single core and write the certified census archive `anc/results_paper_c.json`.

Exact simplex moments for continuous polyhedra. As in [14, App. A], doubling the centred coordinates (1) produces integer vectors $P = 2\mathbf{p} \in \mathbb{Z}^3$, and every facet plane $aX + bY + cZ + d = 0$ of $\mathcal{G}_0(S)$ and of the inner core gem $\mathcal{G}_1(S) = \operatorname{conv} P_S^{(1)}$ is certified in exact integer arithmetic. To compute the exact rational volume $\operatorname{vol}(\mathcal{G})$, solid centroid $\mathbf{c}_{\text{solid}}(\mathcal{G})$, and second-moment covariance matrix $\Sigma_{\text{solid}}(\mathcal{G})$ of any 3-dimensional gem $\mathcal{G}$, we decompose $\mathcal{G}$ into tetrahedra $\Delta_k = \operatorname{conv}\{\mathbf{v}_0, \mathbf{v}_{k,1}, \mathbf{v}_{k,2}, \mathbf{v}_{k,3}\}$ sharing the rational vertex $\mathbf{v}_0 = \frac{1}{2}P_0 \in (\frac{1}{2}\mathbb{Z})^3$. Each tetrahedron has exact rational volume

$$V_k = \frac{1}{6}\left|\det(\mathbf{v}_{k,1} - \mathbf{v}_0,\ \mathbf{v}_{k,2} - \mathbf{v}_0,\ \mathbf{v}_{k,3} - \mathbf{v}_0)\right| \in \mathbb{Q}_{\geq 0},$$

exact first moment

$$\iiint_{\Delta_k} \mathbf{x}\, dV = \frac{V_k}{4}\left(\mathbf{v}_0 + \mathbf{v}_{k,1} + \mathbf{v}_{k,2} + \mathbf{v}_{k,3}\right) \in \mathbb{Q}^3,$$

and exact canonical second moment

$$\iiint_{\Delta_k} x_i x_j\, dV = \frac{V_k}{20}\left(2\sum_{a=0}^{3} v_{a,i}v_{a,j} + \sum_{0\leq a\neq b\leq 3} v_{a,i}v_{b,j}\right) \in \mathbb{Q},$$

where $(\mathbf{v}_{k,0}, \mathbf{v}_{k,1}, \mathbf{v}_{k,2}, \mathbf{v}_{k,3}) = (\mathbf{v}_0, \mathbf{v}_{k,1}, \mathbf{v}_{k,2}, \mathbf{v}_{k,3})$. Summing over all simplices Δ_k yields $\operatorname{vol}(\mathcal{G}) = \sum_k V_k \in \mathbb{Q}$, $\mathbf{c}_{\text{solid}}(\mathcal{G}) = \frac{1}{\operatorname{vol}(\mathcal{G})}\sum_k \iiint_{\Delta_k} \mathbf{x}\, dV \in \mathbb{Q}^3$, and $\Sigma_{\text{solid},ij} = \frac{1}{\operatorname{vol}(\mathcal{G})}\sum_k \iiint_{\Delta_k} x_i x_j\, dV - c_{\text{solid},i}c_{\text{solid},j} \in \mathbb{Q}$ without floating-point rounding. Because the simplicial decomposition partitions the convex body $\mathcal{G}$, these rational integrals are independent of the choice of boundary triangulation.

Complete list of the 33 two-density balanced gems. For completeness, Table 5 lists all 33 order-four magic squares for which $\dim \mathcal{G}_1(S) = 3$ and the solid centroids $\mathbf{c}_0(S)$ and $\mathbf{c}_1(S)$ are strictly anti-parallel, together with their exact rational balancing density increment $\Delta\rho_1/\rho_0 = -\operatorname{vol}(\mathcal{G}_0)c_0/(\operatorname{vol}(\mathcal{G}_1)c_1) > 0$ (Theorem 4.3). Every one of the 33 squares belongs to Dudeney's Group VI.

Table 5: Complete census of the 33 order-four Magic Gems admitting exact two-density "diamond-in-a-diamond" solid balance $\mathbf{c}_{\text{comp}} = \mathbf{0}$ (Theorem 4.3), sorted by increasing excess density ratio $\Delta\rho_1/\rho_0$.

Gem	$\operatorname{vol}(\mathcal{G}_0)$	$\operatorname{vol}(\mathcal{G}_1)$	$\Delta\rho_1/\rho_0$	Gem	$\operatorname{vol}(\mathcal{G}_0)$	$\operatorname{vol}(\mathcal{G}_1)$	$\Delta\rho_1/\rho_0$	Gem	$\operatorname{vol}(\mathcal{G}_0)$	$\operatorname{vol}(\mathcal{G}_1)$	$\Delta\rho_1/\rho_0$
#673	257/3	56/3	5/4	#665	281/3	6	61/13	#697	248/3	28/3	166/11
#502	271/3	6	4/3	#252	233/3	7	88/9	#671	84	2/3	31/2
#45	214/3	6	85/61	#166	93	8/3	21/2	#383	284/3	7	47/3
#50	254/3	22/3	28/19	#158	88	9	57/5	#398	260/3	7	95/6
#307	277/3	22/3	23/15	#168	280/3	7	110/9	#18	71	9	33/2
#49	81	2	2	#672	260/3	4/3	99/8	#627	83	4/3	67/4
#38	263/3	22/3	31/15	#167	90	8/3	27/2	#452	236/3	6	118/7
#47	247/3	22/3	40/19	#199	256/3	22/3	206/15	#604	221/3	26/3	229/10
#261	259/3	7	47/12	#615	244/3	5	14	#226	235/3	7	143/6
#670	244/3	10	103/25	#6	239/3	7	127/9	#626	69	2/3	49/2
#488	277/3	22/3	71/16	#573	251/3	8	44/3	#436	235/3	6	191/6